Embryo-derived brain-resident macrophages sustain sleep-wake circuits

Ali Seifinejad[1#*], Mojtaba Bandarabadi[2], Meriem Haddar[2],
Saskia Wundt[1], Victoria Wingert[3], Anne Vassalli[2], Luciana Hannibal[3], Mehdi Tafti[2],
Gianni Monaco[1*]

[1] Institute of Neuropathology, Faculty of Medicine, University of Freiburg, Freiburg, Germany
[2] Department of Biomedical Sciences, University of Lausanne, Lausanne, Switzerland
[3] Department of General Paediatrics, Adolescent Medicine and Neonatology, Laboratory of Clinical Biochemistry and Metabolism, Medical Center, University of Freiburg, Faculty of Medicine, Freiburg, Germany
#Present address: Department of Biomedical Sciences, University of Lausanne, Lausanne, Switzerland

[*]Correspondence to:
Ali Seifinejad: ali.seifinejad@mail.ch or
Gianni Monaco: mongianni1@gmail.com

Summary

Sleep is a complex behavior regulated by a variety of brain cell types. The roles of brain-resident macrophages, such as microglia and CNS-associated macrophages (CAMs), including those derived postnatally, are not well defined. Here, we investigated the reciprocal interaction of brain-resident macrophages and sleep using multimodal high-throughput transcriptional, electrophysiological and metabolomic profiling in mice. We found that sleep deprivation caused profound transcriptional changes in microglia and CAMs, which were intensified by impaired sleep regulation in the absence of the important sleep-regulatory neuropeptide hypocretin/orexin (HCRT). Depletion in embryonically-derived brain macrophages caused increased sleep in the active period, but reduced its quality, reflected in reduced power of brain sleep oscillations. This was observed both for the Non-REM and REM sleep stages. Subsequent repopulation by postnatal brain macrophages unexpectedly failed to reestablish normal sleep-wake patterns and additionally induced sleep fragmentation. Furthermore, brain macrophage depletion caused excitatory-inhibitory synaptic imbalance, which was resistant to repopulation, and led to increased inhibitory synapses. At the metabolite level, the distinct metabolite profile induced by brain macrophage depletion largely returned to normal after repopulation. Our findings suggest a so far largely unknown interaction between brain-resident macrophages and sleep and emphasizes striking functional differences between embryonic and postnatally-derived brain macrophages, paving the way to future exploration of the role of brain macrophages of different origin in sleep disorders and synaptic connectivity.

Keywords: Microglia; CAM, vigilance states, sleep; HCRT

52 **Introduction**

53 Sleep is a complex behavior essential for the normal functioning of animals, consistently
54 linked to various diseases when compromised(1). Sleep regulation involves circadian and
55 homeostatic processes, determining respectively sleep timing and sleep need(2).

56 Sleep oscillatory patterns rely on the intricate connectivity of the central nervous system (CNS)
57 at synaptic and neurotransmitter levels. Various cell types, primarily neuronal populations
58 located in the hypothalamus, brainstem (BS), and basal forebrain (BF), interact to finely
59 regulate sleep. The expression of synaptic proteins increases during wakefulness and sleep
60 loss, and decreases during sleep(3), and the postsynaptic protein HOMER1A is a well-
61 established core brain molecular correlate of sleep loss (4). Additionally, the release of key
62 neuropeptides and neurotransmitters such as HCRT (also called Orexin), serotonin (5HT),
63 noradrenaline (NA), and acetylcholine across different brain regions actively modulates sleep-
64 wake cycles(5). This intricate interplay manifests in electroencephalographically (EEG)
65 measurable readouts distinguishing wakefulness, non-rapid eye movement sleep (NREMS),
66 and rapid eye movement sleep (REMS), characterized by distinct brain oscillatory activities
67 such as delta waves (0.5-4 Hz) for NREMS and theta waves (6-9 Hz) for REMS in rodents.
68 However, the contribution of non-neuronal cell types, such as brain-resident macrophages, to
69 brain oscillations and sleep architecture remains largely unexplored.

70 Brain-resident macrophages comprising parenchymal microglia and CAMs(6-8), play
71 significant roles in pathology and protecting the CNS from damage(9). Although the function
72 of CAMs in regulating brain function is not well understood, microglia participate in a range of
73 physiological functions including synaptic pruning(10). Microglial cells and leptomeningeal
74 macrophages (as part of the CAMs) are derived from prenatal sources known as
75 erythromyeloid precursors that engraft into the developing CNS(11, 12) and facilitate the
76 establishment of neuronal networks especially in the first postnatal weeks (10). If embryonic
77 microglial cells are depleted in adulthood, they repopulate from surviving endogenous cells
78 (13). D*e novo* establishment of micoglial networks occurs by surviving cells through clonal

expansion (14) and these postnatal-derived microglial cells exhibit a different transcriptional signature (15). However, whether adulthood-derived microglia exhibit functional differences relative to orginal embryo-derived populations is largely unknown.

While a few studies have demonstrated a bidirectional relationship between embryo-derived microglia and sleep/wake states (16-19), a comprehensive understanding of how these two compartments modulate each other is still lacking. Specifically, the transcriptional signature of microglia and CAMs in response to sleep loss remains unknown. Conversely, the extent to which brain-resident macrophages impact sleep EEG activity requires thorough investigation through extensive EEG analysis. Moreover, the influence of brain macrophages on sleep-regulating neurotransmitters, neurochemical content, and synaptic connectivity warrants further exploration. Furthermore, it remains unclear whether adulthood-derived microglia are capable of re-establishing neural circuitries in the same manner as prenatal microglial cells, including synaptic plasticity and neurochemical balance, which are crucial for normal sleep regulation.

Here, we first studied the impact of sleep deprivation on the transcriptional signature of microglia and CAMs. Next, through in-depth analysis, we explored whether absence of embryo-derived microglia and CAMs influences sleep EEG patterns and whether repopulated postnatal microglia and CAMs can normalize these patterns. Finally, we investigated how the absence of microglia and CAMs affects brain network connectivity and neurochemistry.

98 **Results**

99 **Sleep loss markedly alters the transcriptional profile of microglia and CAMs**

100 We first investigated how lack of sleep impacts brain-resident macrophages. Sleep deprivation
101 (SD) has shown to induce functional alterations in microglia(20, 21), however, its impact on
102 the transcriptional profile of microglia and CAMs has not yet been documented. We thus
103 deprived wild-type (WT) mice of sleep for 6 h (starting from light onset) and immediately
104 afterward isolated microglia (CD11b^{+}, CD45^{intermediate}) and CAMs (CD11b^{+}, CD206^{+}, Fig. 1 A-
105 B) from the cortex and hypothalamus, 2 major sleep-regulating centers, and performed gene
106 expression analysis. The control group was not sleep deprived. We extracted RNA and
107 performed bulk RNA sequencing (RNA-seq) to compare the transcriptome between SD and
108 control conditions. After 6 hours SD, no changes were observed in expression of microglial
109 core genes (*Hexb*, *P2ry12*, *Trem2*, and *TMEM119*) across the cortex and hypothalamus
110 (Supplementary Fig. 1A). However, we observed many other differentially expressed genes
111 (DEGs) (110 genes) (Figure 1C). While almost an equal number of genes were differentially
112 regulated in cortex and hypothalamus after SD, we found genes only affected either in the
113 cortex (e.g. *Cul1*, *Ints6l*, and *Ccnl2*) or the hypothalamus (e.g. *Slc1a3*, *Pdia3*, and *Rpn1*)
114 (Supplementary Fig. 2) indicating region-specific microglial response to SD. Gene set
115 enrichment analysis of the DEGs in WT mice revealed an enrichment of pathways related to
116 protein folding, such as 'Positive regulation of protein folding' (Fig. 1D).

117 We next investigated how SD affects the transcriptome of CAMs. As CAMs are not abundant
118 in the brain, we sorted them from the entire brain. Our results revealed that 6 h of SD induced
119 numerous DEGs in CAMs (Fig. 1E). Among them, both the *App* and *Lyve1* genes (Fig. 1F)
120 were previously linked to Alzheimer's disease (AD) pathogenesis (22, 23). Remarkably, *Lyve1*
121 gene expression almost tripled after 6 h of SD. Gene set enrichment analysis of DEGs of
122 CAMs in WT mice revealed enrichment for pathways related to AD, including 'Positive
123 regulation of tau-protein kinase activity' (Fig. 1G).

124 To further understand the effect of sleep on brain-resident macrophages, we additionally,
125 analyzed the transcriptome of microglia and CAM in mice with a disrupted regulation of sleep,

126 the *Hcrt-ataxin-3* transgenic mice (hereafter referred to as Ox-Ataxin mice), which experience
127 HCRT neuronal degeneration during development (24). HCRT neurons play a critical role in
128 waking behaviors that drive sleep need (25). Ox-Ataxin mice represent a model for narcolepsy
129 disease, manifesting excessive daytime sleepiness, fragmentation of wake and sleep.
130 Transcriptional comparison of SD and control conditions in microglia of OX-Ataxin mice
131 resulted in a larger number of DEGs compared to WT mice (270 vs 110 genes) (Figure 1H, I),
132 suggesting that sleep loss significantly increases the transcriptional change in microglia in the
133 mice with disrupted sleep regulatory pathways. Among the DEGs, some were shared between
134 the two mouse lines, however, Ox-Ataxin mice exhibited many DEGs that were not
135 differentially regulated in WT mice in response to sleep loss (e.g. *Naglu*, *Lyz2*, *Rsp9*, *Rps29*,
136 *Stip1*) (Fig. I). We additionally found that SD primarily affects cortical, rather than hypothalamic
137 microglia in Ox-Ataxin mice, indicating that the cortical microglia are more susceptible to
138 vigilance state instability induced by the lack of wake-promoting neuropeptide HCRT
139 (Supplementary Fig. 2). While we did not detect the expression of HCRT receptors in
140 microglia, we observed the expression of downstream circuit receptors, including
141 noradrenaline and serotonin receptors, in microglia. One such gene is the beta-2 adrenergic
142 receptor (*Adrb2*), which is predominantly expressed in hypothalamic microglia compared to
143 cortical microglia (Supplementary Fig. 1B). Gene set enrichment analysis of the DEGs in
144 microglia of Ox-Ataxin mice revealed an enrichment of pathways like "Virion attachment to
145 host cell" (Fig. 1J).
146 Overall, in the two mouse lines, we found microglial genes primarily regulated under the SD
147 condition, such as *Cirbp*, *Ighd*, and *Npnt* (Fig. 1K). Additionally, we found genes that were
148 more expressed in the hypothalamus compared to the cortex (Fig. 1L). Furthermore, we
149 observed that genes such as *Sgk1* and *Pecr* were largely regulated after SD in the
150 hypothalamus but not in the cortex, suggesting structure-specific microglia changes after SD
151 (Fig. 1M). Lastly, we found genes that were exclusively regulated in Ox-Ataxin mice such as
152 *Slc31a2*, *Lyz2*, and *Ccl4* (Fig. 1N).

153 Analysis of SD vs control conditions in CAMs of Ox-Ataxin mice surprisingly revealed a
154 profoundly diminished number of DEGs relative to WT mice (only 6 genes), suggesting that
155 CAMs show a blunted response to sleep deprivation in absence of a functional HCRT system
156 (Fig. 1O).
157 In summary, our data show that sleep significantly influences the transcriptional profiles of
158 brain-resident macrophages, indicating intricate interactions between these two systems. SD
159 induces major changes in the transcriptional profile of microglia and CAM genes involved in
160 disease-related pathways.
161
162 **Repopulated adulthood-derived microglia are deficient in rebuilding normal NREMS**
163 **circuitry**
164 We next examined to what extent embryo-derived brain-resident macrophages contribute to
165 sleep regulation and whether postnatal-derived macrophages can perform the same function.
166 To address this, we depleted microglia from the brains of mice for two weeks using colony-
167 stimulating factor 1 receptor (CSF1R) inhibition via PLX5622 (26), and then allowed them to
168 repopulate for four weeks (Fig. 2A). CSF1 receptor is vital for microglia survival. Antagonizing
169 it severely depletes microglia within three days, and upon the termination of treatment,
170 repopulation can be readily observed within a few days(15). We observed substantial microglia
171 depletion (>86%) after two weeks of PLX5622 treatment, and complete repopulation four
172 weeks after withdrawal (Fig. 2B, C).
173 We recorded EEG signals before depletion (control), after depletion and after repopulation
174 (Fig. 2A). Since CSF1 inhibition also depletes CAMs(27), the effects we report here are due
175 to the depletion of both cell types, which we refer to collectively as MG. Our experimental
176 conditions therefore included control, MG-Dep (microglia/CAM depleted), and MG-Repop
177 (microglia/CAM repopulation). To evaluate the distribution of vigilance states, we employed
178 our standard sleep/wake phenotyping protocol(28), with two days of baseline (which were
179 averaged and presented as one day in the figures) and in the third day mice underwent 6 h of
180 SD (ZT0-ZT6) and 18 h of recovery (Fig. 2D). In baseline conditions, all experimental mice

181 demonstrated the characteristic cycling behavior, with higher levels of wakefulness during the
182 dark period and higher levels of NREMS during the light period and exhibited the increase in
183 NREMS amounts in response to SD (Fig. 2E, F). However, a significant NREMS increase was
184 observed in the baseline dark period when comparing the MG-Dep to the control condition.
185 Interestingly, the repopulation of MG did not normalize this effect (Control: 12.75±0.72 min,
186 MG-Dep: 16.78±0.77 min, MG-Repop: 16.54±0.70 min, mean ± SEM) (Fig. 2E, F, bottom
187 panels). Reciprocally, there was a notable reduction in wakefulness during the dark period
188 (Fig. 2E, F, top panels).
189 To gain insight into sleep homeostatic regulation in different mouse groups and determine
190 whether increased sleep is due to increased need for sleep, we analyzed the time course of
191 NREMS EEG delta power (1-4 Hz, a recognized quantitative readout of sleep need) across
192 our 3-day recordings. All mice groups showed a typical decline in delta power during the light
193 period and a strong rebound after SD, indicating homeostatic regulation of sleep need in all
194 groups (Fig. 2G). However, the buildup in delta power during the baseline dark period was
195 significantly lower in MG-Dep and MG-Repop mice compared to WT mice (Fig. 2G). This
196 attenuation was more pronounced in MG-Repop mice and may be partly related to the
197 increased amount of sleep during the baseline dark period (Fig. 2E, lower panel). In contrast,
198 when mice were exposed to enforced wakefulness (SD), the EEG delta power increase was
199 significantly more pronounced in MG-Dep and MG-Repop than in control conditions, and again
200 this effect was more extensive in MG-Repop than in MG-Dep (Fig. 2G). Altogether, these data
201 indicate impaired buildup of homeostatic sleep need during the waking period.
202 Spectral analysis of NREMS revealed that MG-Dep mice exhibited higher slow-delta (1-2 Hz)
203 activity compared to control mice in baseline light period (Fig. 2H, left). This frequency band
204 appears particularly affected also in MG-Repop mice, as it was significantly increased in the
205 recovery light period following SD (Fig. 2I, left). The fast-delta (3-4 Hz) frequency range was
206 in contrast blunted during both baseline and recovery light periods only in the MG-Dep
207 condition (Fig. 2H, I, left). During the baseline dark period, large delta power blunting was
208 observed in both MG-Repop (1.5-3.5 Hz) and MG-Dep (3-5.5 Hz) conditions. These deficits

209 remained nearly the same during the recovery dark period, indicating that NREMS of both
210 experimental mice appears to be shallower (Fig. 2H, I, right). Collectively, it can be concluded
211 that the presence of MG is necessary for the precise regulation of fast and slow-delta power
212 as a proxy of the sleep homeostatic process. MG repopulation not only fails to restore NREMS
213 regulation but worsens it.
214 To determine whether increased NREMS duration is due to enhanced state initiation
215 (increased number of NREMS episodes) and/or to enhanced state maintenance (increased
216 NREMS episode duration), we conducted a sleep fragmentation analysis. We found that while
217 MG-Dep mice have similar sleep bout duration patterns as the control condition, MG-Repop
218 mice showed a larger number of shorter NREMS bouts (16 seconds [Control: 6.7±0.63, MG-
219 Dep: 6.8±0.7, MG-Repop: 9.84±1.12]) and 64 seconds [Control: 12.12±1.15, MG-Dep:
220 11.02±0.81, MG-Repop: 17.63±1.2]) and fewer longer NREMS bouts (>256 seconds [Control:
221 1.96±0.28, MG-Dep: 1.74±0.33, MG-Repop: 0.62±0.17]), suggesting a strong destabilization
222 of NREMS in the MG-Repop brain (Fig. 2J).
223 During NREMS, brief bursts of brain activity in the 9-16 Hz frequency range, called spindles,
224 are generated by thalamo-cortical interactions and play roles in processes such as learning,
225 memory, and cognition(29). To determine if MG depletion and repopulation influence spindle
226 generation, we quantified spindle rate during NREMS episodes and found a significantly
227 reduced spindle rate in MG-Dep mice compared to the control condition (Fig. 2K, L; see
228 “Methods”). In contrast to other features of NREMS, MG repopulation was found to normalize
229 the occurrence rate of spindle events, indicating that MG repopulation partially rescues the
230 circuit deficits seen after MG depletion.
231 Altogether, these data suggest that embryo-derived MG are an integral part of NREMS
232 establishment and maintenance, and repopulated postnatal MG largely fail to fulfill the normal
233 NREMS regulatory functions of embryo-derived MG.
234
235 **Depletion of microglia prolongs REMS and degrades its quality**

236 Different neural pathways and neurotransmitters regulate REMS compared to NREMS.
237 However, the role of MG in the regulation of REMS is not well understood. We quantified
238 REMS amount across the dark/light periods and found that MG-Dep mice display more REMS
239 compared to the control and MG-Repop conditions during the baseline dark period (Control:
240 0.67±0.1, MG-Dep: 1.17±0.21 min/h, mean ± SEM). However, in contrast to NREMS, MG
241 repopulation corrected the abnormal expression of REMS (MG-Repop: 0.61±0.13 min/h) (Fig.
242 3A, B). To investigate if the increase in REMS is due to the consolidation of this state, we
243 performed fragmentation analysis and found that the number of shorter REMS bouts (8 s) is
244 largely decreased (Control: 8.7±2.05, MG-Dep: 2.8±1.2, MG-Repop: 8.8±3.3) and longer
245 bouts (>2 min) are increased (Control: 1.5±0.8, MG-Dep: 6.1±1.1, MG-Repop: 4.71±1.4, mean
246 ± SEM) (Fig. 3C) in MG-Dep mice, suggesting stabilization of REMS in the absence of MG.
247 Theta oscillations dominate the EEG signal during REMS, where theta phase dynamically
248 modulates gamma amplitude in hippocampal and cortical networks(30). We next investigated
249 the contribution of MG in theta oscillations and theta-gamma interactions. Spectral analysis of
250 REMS revealed a significant dampening of theta (6-8 Hz) power in MG-Dep mice during the
251 baseline dark period (Fig. 3D), which was restored after MG repopulation. We also found that
252 the theta-gamma coupling is significantly reduced in the MG-Dep condition compared to the
253 control. Although MG repopulation attempts to bring it back to the normal level, it fails
254 significantly (Fig. 3E, F).
255 Altogether, these findings suggest that the presence of MG is necessary for the normal
256 expression of REMS.
257
258 **Microglia contribute to the maintenance of active wakefulness**
259 The quality of prior wakefulness contributes to the expression of both NREMS and REMS.
260 Along these lines, a specific sub-state of prior wakefulness was recently proposed to drive
261 NREMS need (25), and some aspects of wakefulness may functionally substitute for REMS
262 (31). To investigate how wakefulness is expressed in our experimental conditions, we
263 performed a dynamic analysis of the full waking EEG spectrum across three recording days.

This global analysis revealed differential expression of the higher waking frequency bands during light-dark cycles across three days, and most notably during enforced wakefulness (SD). As suggested in Figure 4 (Fig. 4A), both MG-Dep and MG-Repop mice exhibit a large dampening of the lower gamma (≈45-55 Hz) band during the baseline dark period, which is exacerbated during the recovery dark period. Additionally, the MG-Dep mice exhibit a large blunting of the higher gamma band (≈70-90 Hz) during SD, which partially normalizes after MG repopulation. To better quantify the lower frequency bands, we performed PSD analysis and found that MG-Dep mice exhibit a large increase in slow delta (1.35-1.75 Hz) activity compared to the control mice (Fig. 4B).

Mice spend a portion of their waking time engaged in exploratory and motivated behaviors, such as running, nest building, or drinking, often referred to in rodents as "active wakefulness". These behaviors are associated with the EEG signature called "theta-dominated wakefulness" (TDW 6.0-9.5 Hz), which has been suggested to be the principal driver of the sleep homeostat (25). We quantified TDW in our mice and found a large decrease in its amount in both MG-Dep and MG-Repop mice during the baseline dark period (Fig. 4C, D). This reduction was more pronounced in MG-Repop mice, which was also seen during SD (Fig. 3C, E). TDW is associated with heightened gamma activity. We analyzed the time course of gamma activity during wakefulness and found an increase in slow (32-45Hz) frequency bands in the MG-Repop condition compared to the controls (Fig. 4F). The increase in these frequency bands in MG-Repop mice is also apparent on time-frequency heat maps in Figure 4A.

Overall, these data suggest a significant imbalance in the theta/gamma-rich waking state in both the MG-Dep and MG-Repop conditions, and appearance of heightened gamma activity after MG repopulation.

Disrupted balance of synaptic signaling upon microglial depletion and repopulation

Sleep is associated with changes in synaptic plasticity(32) and microglia play a substantial role in synaptic functions, which are dependent on neuronal activity and vigilance states (VS)(33). To investigate whether MG depletion and repopulation induce changes in brain

292 network connectivity at the synaptic level, we analyzed a subset of excitatory and inhibitory
293 synaptic density proteins that are involved in sleep regulation, (e.g., the core brain molecular
294 correlate of sleep loss, HOMER1) in the brains of our experimental mice.
295 Using an ImageJ macro, we counted the number of synapses on cortical and hypothalamic
296 neurons (Fig. 5A, B) and found that the number of excitatory VGLUT1-HOMER1 synapses on
297 $NEUN^+$ cortical neurons was significantly reduced in both MG-Dep and MG-Repop conditions.
298 This reduction was more noticeable in MG-Repop mice (Fig. 5C). Interestingly, this effect was
299 regulated at the postsynaptic level (HOMER1-associated, Fig. 5D) rather than the presynaptic
300 level (VGLUT1-associated, Fig. 5E). Recently, cortical PV neurons have been proposed to be
301 responsible for homeostatic sleep regulation(34). We found that the number of parvalbumin
302 (PV)-originated(35) Synaptotagmin-2-Gephyrin (Syt2-Geph) inhibitory synapses on the
303 cortical $NEUN^+$ neurons was significantly increased under the MG-Repop condition (Fig. 5F,
304 G). This increase could possibly be due to an increase in the activity of PV neurons, as we
305 found that the number of VGLUT1-HOMER1 excitatory synapses on PV neurons was
306 significantly increased under both MG-Dep and MG-Repop conditions (Fig. 5H, I). We
307 additionally investigated the changes in the count of VGLUT1-HOMER1 synapses on
308 representative hypothalamic neurons (HCRT) and found a significant decrease in the number
309 of VGLUT1-HOMER1 synapses on HCRT neurons in both MG-Dep and MG-Repop conditions
310 (Fig. 5J, K).
311 To further investigate changes in network connectivity in the brains of MG-Dep and MG-Repop
312 mice, we analyzed additional synaptic markers and sleep-specific neurotransmitter receptors
313 (e.g., receptors of monoaminergic systems and neuropeptides) on RNA extracted from cortical
314 samples of these mice. Our bulk analysis revealed that some general synaptic markers, such
315 as *Synaptophysin I* (*Syp*), are largely downregulated in both experimental mice, while *Slc17a7*
316 (encoding Vesicular glutamate transporter 1) and *Homer1* genes are significantly
317 downregulated in the cortex of the MG-Repop condition. Among the specific neurotransmitter
318 markers analyzed, the adrenergic receptor family (e.g. *Adrb2*, *Adra2a*, *Adrb3*, and *Adra1a*)
319 genes showed a tendency to be less expressed in both MG-Dep and MG-Repop conditions,

320 with a marked decrease in the expression of the *Adra2a* gene. Additionally, we observed a
321 reduction in expression of *Cholinergic receptor muscarinic 2* (*Chrm2*) and the serotonergic
322 receptor *5-Hydroxytryptamine receptor 1A* (*Htr1a*) genes, which mainly occur in the brain of
323 MG-Repop mice (Fig. 5L).
324 Taken together, these data suggest that brain connectivity at the synaptic level is largely
325 impaired following the depletion of brain-resident macrophages. Repopulating the brain with
326 these macrophages not only failed to normalize connectivity but, in many cases analyzed,
327 worsened it.
328
329 **Neurotransmitter release is largely restored after the repopulation of resident**
330 **macrophages**
331 Synapses, in addition to providing structural connections in the brain, play a crucial role in
332 transmitting neurotransmitters essential for the function of complex neural systems. We
333 therefore questioned whether the levels of essential neurotransmitters involved in sleep
334 regulation are affected by the depletion and repopulation of brain-resident macrophages. We
335 conducted targeted metabolomics to analyze the neurotransmitter content and metabolite
336 reservoir of the cortex, target of most neurotransmitters and region where EEG signals are
337 acquired. Assessment of neurotransmitter content was performed using chromatography with
338 tandem mass spectrometry (LC-MS/MS) in the brain of control, as well as MG-Dep and MG-
339 Repop mice. We found that pharmacological depletion of MG led to a distinct clustering of
340 metabolites, as indicated by principal component analysis (PCA) (Fig. 6A). This suggests that
341 MG plays an important role in maintaining the overall metabolic composition of the cortex. MG
342 repopulation however restored the cortical submetabolome to a pattern similar to the one
343 observed under control experimental conditions (Figure 6A). Univariate analysis revealed a
344 reduction in norepinephrine upon MG depletion, which was restored after repopulation (Figure
345 6B). The concentrations of acetylcholine, choline, dopamine, and serotonin remained
346 unchanged between the experimental conditions, with a slight tendency to decrease in MG-
347 Dep condition.

348 Furthermore, we observed that MG depletion led to a marked reduction of L-2-amino adipic
349 acid (L-2-AAA), which was only partially recovered after repopulation (Figure 6B). We also
350 analyzed the precursors of neurotransmitters and found a significant decrease in the amino
351 acids L-serine and asparagine under depleted condition, which could be restored upon MG
352 repopulation (Figure 6C). Similarly, there was a trend towards decreased glycine and L-
353 glutamic acid content (Figure 6C).
354 Taken together, our data suggest that while network connectivity is significantly impaired in
355 MG-Dep condition and resistant to MG repopulation, the underlying substrates
356 (neurotransmitters and metabolites) are largely restored after MG repopulation.
357

358 **Discussion**

359 In this study, we investigated the reciprocal interaction between sleep and brain-resident
360 macrophages. We first analyzed the transcriptional changes in microglia and CAMs in
361 response to sleep loss. While the effects of sleep on oligodendrocytes(36) and astrocytes(37)
362 have been documented, its effects on brain-resident macrophages are less explored. We
363 show that lack of sleep induces significant transcriptional changes in both MG and CAMs,
364 These changes are further amplified when the normal sleep-regulatory system is impaired, as
365 seen in the narcolepsy OX-Ataxin mouse model. We found that the altered genes are involved
366 in disease-related pathways including regulation of protein folding and Tau-protein kinase
367 activity. These pathways are involved in neurodegeneration(38, 39), and the role of microglia
368 in sleep loss-associated neurodegeneration is under investigation(17, 40). Our data showed
369 that removing the important sleep-regulating neuropeptide, HCRT, induces massive
370 transcriptional changes in both microglia (increased number of DEGs) and CAMs (decreased
371 number of DEGs). Previous studies have shown that a null mutation in the *Hcrt* gene in an AD
372 mouse model leads to a significant reduction in Aβ brain pathology(41), and human narcolepsy
373 patients who lack a functional HCRT system display reduced amyloid burden(42). It can be
374 speculated that this effect is mediated by either microglia or CAMs. Further investigations are

375 warranted to decipher these interactions. We additionally found region-specific transcriptional
376 response to sleep loss in microglia highlighting that local microglia differentially participate in
377 neural functioning of the brain as previously suggested(43, 44).
378 In a reciprocal analysis, we also investigated whether embryo-derived MG contribute to sleep
379 regulation, and whether postnatal-derived MG serve a similar role. We demonstrate that MG
380 depletion has a significant impact on the homeostatic regulation of sleep. The brain circuits
381 most vulnerable to microglia depletion and repopulation, causing the changes in sleep EEG
382 that we document, are still unknown. However, changes in slow-delta activity in NREM sleep,
383 state stabilization and reduced theta power in REMS, as well as changes in waking slow-delta
384 activity, were reported in mice with defects in hypothalamic HCRT and brainstem serotonergic
385 and noradrenergic systems(25, 28, 45, 46). This is suggestive of functionally important local
386 interactions between microglial populations and sleep regulating circuits, as mentioned above.
387 We showed that the changes in sleep patterns after MG depletion are not fully reversed after
388 MG repopulation. Previous studies have shown that the brain global transcriptomes are little
389 influenced by repopulated microglia(15). Furthermore, it has been suggested that after MG
390 repopulation, neuroprotection is achieved through IL-6 induction by neurons(47). Other
391 studies reported full functionality of retinal microglia after repopulation, including continuous
392 retinal surveillance, maintenance of synaptic structure, and normal behavioral and
393 physiological responses to retinal injury (48). However, our data reveal that MG repopulation
394 not only fails to completely restore various aspects of sleep regulation, but in some cases
395 exacerbates altered parameters, such as fragmentation of NREMS and dysregulation of sleep
396 need. This demonstrates striking funtional differences between microgial cells derived from
397 pre-or postantal sources. We speculate that not all microglia-neuronal interactions are
398 properly reestablished by adulthood-derived microglia after repopulation. Whether a longer
399 repopulation period might correct the abnormalities observed in our analysis warrants further
400 investigation. We observed a significant imbalance between excitatory and inhibitory
401 synapses after depletion of embryo-derived microglia and after repopulation with adult
402 microglia, with a notable increase in inhibitory synapses following repopulation. Studies in

403 juvenile mice prevously reported that microglia depletion in the developing brain significantly
404 increases the number of both excitatory (VGLUT1-HOMER1) and inhibitory (Syt2-Gephyrin)
405 synapses on cortical neurons, an effect that persisted after repopulation until P30. However,
406 in the adult (P60) brain, synapse density returned to normal control levels, suggesting that
407 depleting microglia during development causes long-lasting, albeit not permanent, effects(49).
408 Our data, however, show that depleting microglia in adulthood, and then repopulating them,
409 induces different results, with a reduction in excitatory synapses in both MG-Dep and MG-
410 Repop conditions, and an increase in inhibitory synapses in MG-Repop conditions. In the
411 developing brain, it has been suggested that MG-Dep impairs synaptic pruning processes and
412 alters related gene expression(10, 49). Whether the same process or any specific pathways
413 are induced by MG depletion and repopulation in the adult brain, such as aberrant reactivation
414 of developmental programs(50), remains to be found.
415 Furthermore,other studies have suggested that microglia play a role in restraining excessive
416 neuronal activation that cannot be sufficiently suppressed by inhibitory neurons alone(51). Our
417 results suggest that embryo-derived microglia also control excessive activity of inhibitory PV
418 neurons, but the reasons why this is not corrected with adulthood-derived microglia remain to
419 be investigated.
420 Deficient synaptic neurotransmission was proposed as a potential cause for abnormal sleep
421 regulation(52). We found here an imbalanced neurotransmitter and metabolite content of the
422 brain in mice devoid of prenatal microglia. It appears that norepinephrine neurotransmission
423 is particularly sensitive to MG deficiency, as both the levels of norepinephrine metabolites and
424 the corresponding receptors are significantly affected by MG depletion. Norepinephrine is
425 implicated in both wakefulness(53) and sleep regulation(54-56), and it has been suggested
426 that microglial surveillance process relies heavily on norepinephrine signaling(57, 58).
427 Additionally, we observed a decrease in the expression of neurotransmitter precursors such
428 as L-serine, which was mirrored by changes in the concentrations of glycine, asparagine, and
429 glutamic acid. Previous studies have proposed serine as a link between metabolism and

430 neurotransmission (59), and serine serves as a precursor for synthesizing ceramide (60),
431 which has been suggested to be essential for maintaining stable wakefulness (61).
432 Our findings indicate that MG affect vigilane state regulation via multiple pathways and play
433 a more substantial role in maintaining the physical connectivity of brain networks rather than
434 neurochemical connectivity, as MG repopulation largely restores metabolites but not
435 synapses. To gain a detailed understanding of MG regulation of sleep, it will be necessary to
436 explore local specific microglial depletion, and disruption of microglia-neuron interactions
437 using inducible systems. Additionally, investigating the separate contributions of microglia and
438 CAMs in sleep regulation using Cre lines under the promoter of *Hexb* (62) and *Mrc1* (63)
439 genes, respectively, would be a starting point. The observed vigilance state phenotypic
440 alterations may also be influenced by disruptions in central factors (such as protein
441 phosphorylation orchestrated by microglial TNF-α)(16), and peripheral players (since CSF1R
442 inhibition also effects circulating and tissue macrophages)(64) warranting further
443 investigations. Overall, our results shed new light on the complex interaction between the
444 neuroimmune system and sleep regulation, and it paves the way for future investigations in
445 this important physiopathological field.
446

447 **Data availability**

448 All data are available from the corresponding author upon reasonable request. Bulk RNA
449 sequencing datasets were deposited into the Gene Expression Omnibus database under
450 accession number XXXXX and are available at the following URL: XXXXXXXX.

451 **Acknowledgements**

452 AS was supported by Novartis Foundation for medical-biological Research (#23B079). MB
453 was supported by the Swiss National Science Foundation (grant 190605). MT was supported
454 by Swiss NSF (grant 201235), and the State of Vaud (Faculty of Biology and Medicine,

455 University of Lausanne). AV was supported by the Swiss National Science Foundation (grant
456 31003A_182613).

457 **Author contributions**

458 AS conceptualized and designed the study. AS, MH, SW, VW and LH performed
459 experiments. AS, GM, MB and LH analyzed data. AS, GM, AV, MT, MB, and LH wrote the
460 manuscript.
461
462
463 **Declaration of interests**

464 The authors declare no competing interests.
465

466 **Methods**

467 **Animals.** Wild type (C57BL/6J) and Ox-ataxin-3 transgenic mice were used in this study. All animals
468 were between 12 and 14 weeks old during the time of experiments and animal experiments were
469 approved by the Ministry for Nature, Environment and Consumers` Protection of the state of Baden-
470 Württemberg and were performed in accordance to the respective national, federal, and institutional
471 regulations. At all times, care was taken to minimize animal discomfort and avoid pain.
472
473 **Microglia and CAM isolation and flow cytometry.** Mice brains were collected and microglia were
474 enriched using density gradient separation and were prepared as described previously (65, 66). The
475 cell suspension was then incubated with Fixable Viability Dye eFluor® 780 (1:1000, 65-0865-14,
476 Invitrogen) for 10 min at 4 °C. Subsequently, the following antibodies were used: antiCD11b (1:200,
477 clone M1/70, 101235 Biolegend), anti-CD45 (1:200, clone 30-F11, 103108 BioLegend), anti-CD11c
478 (1:100, 12-0114-81, Invitrogen), anti-Gr1 (1:200, 108408, Biolegend) and anti-CD206 (1:200, 141708,
479 Biolegend). Cell sorting for RNA-seq was performed on a MoFlo Astrios (Beckman Coulter).
480
481 **Total RNA extraction.** Total RNA was extracted from FACS sorted mouse brain cells stabilized in
482 RNAprotect buffer according to the "Purification of total RNA from animal and human cells" protocol of
483 the RNeasy Plus Micro Kit (QIAGEN, Hilden, Germany).
484 In brief, cells were stored and shipped in buffer RNAprotect at 2-8 °C. After pelleting by centrifugation
485 for 5 minutes at 5,000 x g, the RNAprotect was replaced by 350 µl buffer RLT Plus and the samples
486 were homogenized by vortexing for 30 seconds. Genomic DNA contamination was removed by using
487 gDNA Eliminator spin columns. Next one volume of 70 % ethanol was added and the samples were
488 applied to RNeasy MinElute spin columns followed by several wash steps. Finally the total RNA was

489 eluted in 12 µl of nuclease free water. Purity and integrity of the RNA was assessed on the Agilent 2100
490 Bioanalyzer with the RNA 6000 Pico LabChip reagent set (Agilent, Palo Alto, CA, USA).
491
492 **RNA sequencing.** The SMARTer Ultra Low Input RNA Kit for Sequencing v4 (Clontech Laboratories,
493 Inc., Mountain View, CA, USA) was used to generate first strand cDNA from approximately 1 ng total-
494 RNA. Double stranded cDNA was amplified by LD PCR (13 cycles) and purified via magnetic bead
495 clean-up. Library preparation was carried out as described in the Illumina Nextera XT Sample
496 Preparation Guide (Illumina, Inc., San Diego, CA, USA). Thereby 150 pg of input cDNA were tagmented
497 (tagged and fragmented) by the Nextera XT transposome. The products were purified and amplified via
498 a limited-cycle PCR program to generate multiplexed sequencing libraries. For the PCR step 1:5
499 dilutions of the unique dual indexing (i7 and I5) adapters were used. The libraries were quantified using
500 the KAPA Library Quantification Kit - Illumina/ABI Prism User Guide (Roche Sequencing Solutions, Inc.,
501 Pleasanton, CA, USA). Equimolar amounts of each library were sequenced on an Illumina NextSeq
502 2000 instrument controlled by the NextSeq 2000 Control Software (NCS) v1.4.0.39521, using one 50
503 cycles P3 Flow Cell with the dual index, single-read (SR) run parameters. Image analysis and base
504 calling were done by the Real Time Analysis Software (RTA) v3.9.2. The resulting .cbcl files were
505 converted into .fastq files with the bcl2fastq v2.20 software. RNA extraction, library preparation and
506 RNAseq were performed at the Genomics Core Facility "KFB - Center of Excellence for Fluorescent
507 Bioanalytics" (University of Regensburg, Regensburg, Germany; www.kfb-regensburg.de). Bulk RNA-
508 seq data was aligned with STAR v2.7.10a (67) to the mouse reference genome Gencode M26 (68).
509 Counts were obtained from the bam files with the tool featureCounts v2.0.3. Genes with count
510 expression higher than 5 in at least 3 samples were kept for the differential expression analysis.
511 Differential expression was performed using the limma trend method (69) on the log2 counts per million
512 (CPM) values. Venn diagrams and Volcano plots were generated with the R packages limma and
513 EnhancedVolcano, respectively. Enrichment analysis was performed using ShinyGO (70).
514
515 **Gene expression analysis.** For qPCR analysis, RNA extracted from the cortical samples of control,
516 MG-Dep and MG-Repop mice. RNA was extracted using RNeasy micro kit (74004) and cDNA synthesis
517 was performed using random hexamer primers and M-MLV Reverse Transcriptase Promega kit
518 (M3682). SYBR green-based and Taqman probes were used to detect the gene expression. The assay
519 was performed using a LightCycler480 (Roche).
520
521 **Immunofluorescence and synapse counting**. Mice were anesthetized with ketamine (100 mg per kg
522 body weight) and xylazine (10 mg per kg body weight) followed by perfusion with 1× PBS. For histology,
523 brains were kept overnight in 4% paraformaldehyde (PFA). Brains were then dehydrated in 30%
524 sucrose for about 48 hours and then snap-frozen on dry ice. Cryosections (14µm for synapse counting
525 and 20µm for microglia and CAM staining) from brain tissue were prepared as free floating in PBS. The
526 following antibodies were used to stain microglia, CAM and synapses: Rabbit-anti-IBA1 (ab178846,
527 abcam), Rat-anti-CD206 (Biorad MCA2235), Goat-anti-Collagen type 4 (Millipore AB769), anti-NEUN
528 (ab177487, ab104224, abcam), anti-VLUT1 (135304, synaptic system), anti-HOMER1 (ABN37,

529 Millipore), anti-Gephyrin (147318, synaptic system), anti-Synaptotagmin-2 (ZDB-ATB-081002-25,
530 ZFIN), anti-Parvalbumin (MAB1572, Merck) and anti-HCRT-A (SC-8070). The DAPI was used to stain
531 the nucleus. Rat-anti-CD206 and Goat-anti-Collagen type 4 antibodies were incubated for 48 hours at
532 4 °C to have high quality staining. Iba1 antibody was incubated overnight at 4 °C and the primary
533 antibodies to detect synapses were incubated for 1.45hr at room temperature. The brain cuts were
534 incubated with secondary antibodies for 1-2 hours at room temperature. Fluorescence imaging was
535 performed with TCS SP8 X (Leica Microsystems). Imaging of synapses was performed using 63X
536 objective with zoom factor 8. Iba1^{+} cells were counted using Fiji. Synapse analysis and quantification
537 were conducted using Fiji macro developed previously (71) with little modifications.
538
539 **Quantitative profiling of metabolites by liquid chromatography and mass spectrometry (LC-**
540 **MS/MS).** Mice brain tissue biopsies were thawed and homogenised with ice-cold PBS supplemented
541 with 1% protease inhibitor cocktail (Sigma Nr. P8340-5ML), using a cordless pestle motor and
542 disposable pellet mixers (VWR Nr. 47747-366). Buffer volume was adjusted to reach a target of 0.1 to
543 0.3 mg wet-tissue/mL lysis buffer. Whole tissue homogenates were aliquoted for downstream
544 measurement of total protein concentration, flash-frozen and stored at -80 °C. Sulfur-containing
545 metabolites as well as creatinine, S-adenosylmethionine and S-adenosylhomocysteine were
546 determined according to a previously published procedure (72, 73). Lactate, TCA and glycolysis
547 intermediates and other organic acids, and folates were determined as described in previous work (74).
548 Amino acids and neurotransmitters were determined using a previously described protocol (75, 76). A
549 commercially available standardized amino acid mixture was utilized to generate a calibration curve for
550 amino acids (Amino acid standards, physiological, Sigma, Nr. A9906-10ML). Calibration curves for all
551 other metabolites were prepared from individual stock solutions prepared in house. Quantitation
552 accuracy was examined by monitoring homocysteine and methylmalonic acid concentrations in an
553 external quality control, namely, the Control Special Assays in Serum, European Research Network for
554 the evaluation and improvement of screening, diagnosis, and treatment of Inherited disorders of
555 Metabolism (ERNDIM) IQCS, SAS-02.1 and SAS-02.2 from MCA Laboratories, Winterswijk,
556 Netherlands. For all other metabolites, quantitation trueness was tested by examining metabolite
557 concentrations in plasma from a previously validated sample isolated from a healthy control individual
558 with respect to standard reference ranges, using the same calibration curves and LC-MS/MS running
559 conditions. Quantification of metabolites was carried out with Analyst® 1.7.2 software, 2022 AB Sciex.
560
561 **Treatments.** In order to eliminate cells dependent on CSF1R (MG) mice were administered a CSF1R
562 inhibitor called PLX5622 (Plexxikon). The inhibitor was combined with AIN-76A standard chow at a
563 concentration of 1,200ppm (Research Diets) and the mice were given unrestricted access to it for two
564 weeks. The control group received AIN-76A standard chow without any modifications. After two weeks
565 the PLX5622 food was replaced with control food to start repopulation of MG.
566
567 **Mice surgery, data acquisition and vigilance state analysis.** Mice surgery and data acquisition were
568 performed as previously described (28). MATLAB scripts were created to quantify various parameters

related to wakefulness, NREMS and REMS. These parameters include time distribution and amount of episodes, as well as the fragmentation of vigilance states, all of which were defined based on previously established criteria (28). TDW analysis was conducted following the method described by Vassalli and Franken (25).

Power spectral analysis. Using Somnologica-3TM (Medcare) software, each 4 s epoch of the EEG signal was subjected to discrete Fourier transform to determine EEG power density (spectra 0–90 Hz at a frequency resolution of 0.25 Hz). We used artifact-free, same-state–flanked 4 s epochs to calculate the mean EEG spectral profiles for each behavioral states and time intervals. To account for differences among animals in absolute EEG power, the mean values of spectral profiles were converted into percentages relative to a baseline EEG power reference value of 100%. This reference value was determined for each mouse by summing the power within the frequency range of 0.75–47.5 Hz across all states and throughout the first day of baseline recordings. To control for differences in the amount of wakefulness, NREMS and REMS, this reference was weighted so that the relative contribution of each state was identical for all mice (77). Time-frequency heatmaps of EEG power during wakefulness were generated using methods described previously (78).

Time-course analysis. To examine the dynamic changes of EEG power within specific frequency ranges throughout the day and night, the time-course of the activity of that frequency band was computed for 4 s epochs scored as state of interest (NREMS, REMS and wake). For this purpose, the epochs for each state were divided into percentiles, ensuring that each percentile contained a roughly equal number of epochs. The number of percentiles for NREMS and REMS were: 12 for light periods, 6 for dark periods, and 8 for the 6-h light period after SD; for waking state: 6 for light periods, 12 for dark periods, 8 for the 6-h light SD, and 4 for the 6-h light after SD. The average EEG power within the specified frequency range was computed for each percentile, and subsequently normalized based on the type of analysis. This normalization was either done relative to the total power of the baseline state or with respect to the power achieved within the delta frequency band during slow-wave sleep at ZT8-12. Like power density analysis, single epochs were excluded and only power values of the epochs that themselves, as well as the two adjacent ones, were scored as artifact-free same-state were included in the analysis.

Theta-gamma cross-frequency coupling. We used the modulation index (MI) to measure the theta-gamma phase-amplitude coupling (30, 79). Using finite impulse response filters with an order equal to three cycles of the low cutoff frequency, we first bandpass-filtered EEG signals into theta (6-11 Hz) and fast-gamma (54-90 Hz) in both forward and reverse directions to eliminate phase distortion. We then estimated instantaneous phase of theta and the envelope of fast-gamma using the Hilbert transform. Theta phase was discretized into 18 equal bins (N=18, each 20°) and the average value of fast-gamma envelope within each bin was calculated. The resulting phase-amplitude histogram (P) was compared with a uniform distribution (U) using the Kullback-Leibler distance, $D_{KL}(P,U) = \sum_{j=1}^{N} P(j) * log[P(j)/U(j)]$, and normalized by $log(N)$ to obtain the modulation index, $MI = D_{KL} / log(N)$. To explore

possible coupling patterns between different pairs of low and high frequency bands, we used the comodulogram analysis (79). We considered 16 frequency bands for phase (1-18 Hz, 1-Hz increments, 2-Hz bandwidth), and 14 frequency bands for amplitude (15-90 Hz, 5-Hz increments, 10-Hz bandwidth). MI values were then calculated for all these pairs to obtain the comodulogram graph.

Detection of sleep spindles. NREMS spindles were detected automatically using an optimized wavelet-based method as previously described (29). Briefly, the power of EEG signals within 9-16Hz was estimated using the complex B-spline wavelet function, and smoothed using a 200 ms Hanning window, and then a threshold equal to 3 SD (SD: standard deviation) above the mean was applied to detect the potential spindle events. Events shorter than 400 ms or longer than 2 s were discarded. Using band pass-filtered EEG signals in the spindle range (9–16 Hz), we automatically counted the number of cycles of each detected event and excluded those with <5 cycles or more than 30 cycles. To discard artefacts, events with a power in the spindle band lower than 6–8.5 Hz or 16.5–20 Hz power bands were not included.

Statistical analysis. The specific number (n) of replicates employed in each experiment is provided in the corresponding figure legends. The individuals responsible for conducting SD and scoring the sleep recordings were unaware of the genotype of the animals, ensuring blinding during these procedures. The results are presented as mean ± SEM or mean ± SD. Statistical analyses were conducted using GraphPad Prism. The significance of comparisons was determined using one- or two-way ANOVA or mix effect model followed by relevant post hoc tests and are reported in the figure legends.

635 **Figure legends**

636 **Figure 1. Large transcriptional changes in the microglia and CAMs of WT and Ox-Ataxin**
637 **mice after SD** (**A**) (Left) Representative confocal image of parenchymal microglia (IBA1$^+$,
638 green) and perivascular (yellow arrowheads) and meningeal (white arrowheads) CAMs (IBA1$^+$
639 and CD206$^+$, red). (Right) CAMs are positive for CD206 protein expression and are found in
640 the collagen (Col) IV$^+$ perivascular and meningeal compartment. (**B**) Microglia were sorted as
641 CD11b$^+$; CD45^{Intermediate} populations, separately from the cortex and hypothalamus of WT and
642 Ox-Ataxin-Tg mice. CAMs were sorted as CD11b$^+$ and CD206$^+$ populations from the whole
643 brain of both genotypes. (**C**) Heatmap representation showing differentially expressed genes
644 in microglia from hypothalamus and cortex of WT mice under SD or control conditions. Each
645 column represents microglial gene expression from one individual mouse, with 4-5 mice per
646 group. Linear color scale. (**D**) Gene set enrichment analysis for DEGs in microglia of WT mice.
647 (**E**) Heatmaps depicting DEGs in CAMs of WT mice under SD or control conditions. Each
648 column represents CAM gene expression from one individual mouse, with 4-5 mice per group.
649 Linear color scale. (**F**) Bar plots depicting *App* and *Lyve-1* gene expression under SD or control
650 conditions in CAMs of WT mice. Values are mean ± SEM, n=4-5 (t-test, *P < 0.05; **P < 0.01;
651 ***P < 0.001). (**G**) Gene set enrichment analysis for DEGs in CAMs of WT mice. (**H**) Heatmaps
652 depicting DEGs in microglia from hypothalamus and cortex of Ox-Ataxin mice under SD or
653 control conditions. (**I**) Venn diagram depicting the numbers of differentially regulated and
654 overlapping genes between microglia of WT and OX-Ataxin mice. Red and blue represent up-
655 and down-regulated genes, respectively. (**J**) Gene set enrichment analysis for DEGs in
656 microglia of Ox-Ataxin mice. (**K**, **L**, **M** and **N**) Radar plots representing DEGs in microglia of
657 cortex (Cx) and hypothalamus (Hy) in WT (green dots) and Ox-Ataxin (blue dots) mice under
658 SD (white, top) or control (noSD) condition (yellow, bottom). (**O**) Heatmaps depicting DEGs
659 between the SD and control groups in CAMs of Ox-Ataxin mice. Each column represents CAM
660 gene expression from one individual mouse, with 4-5 mice per group. Linear color scale. The
661 number of DEGs in response to sleep loss in CAMs of Ox-Ataxin mice is markedly diminished
662 relative to WT mice

663

664 **Figure 2. Essential role of MG in regulation of NREMS and associated EEG oscillations.**
665 (**A**) Schematic illustration of the experimental procedure conducted on adult mice to assess
666 the brain's electrical activity using EEG. Recordings prior to PLX5622 drug administration
667 served as controls. Mice were then fed PLX5622-containing food during 2 weeks. During the
668 final 3 days of this 2-week period, a 2nd series of recordings was conducted. Following
669 PLX5622 treatment, mice were provided control food for 4 weeks. After 4 weeks under normal
670 food, a 3rd recording was performed. All 3 recordings were performed on the same mice. (**B,**
671 **C**) PLX5622 substantially depleted the microglia from the brain within 2 weeks (compare
672 control and MG-Dep). Return to normal food repopulated microglia into the brain after 4 weeks
673 (compare MG-Dep and MG-Repop). (**D**) Recording paradigm. The first 2 days of recordings
674 served as baseline, averaged as one day. The 2nd day consisted of 6 h SD followed by 18 h
675 of recovery. (**E**) Time-course of vigilance states; Wakefulness (top) and NREMS (bottom).
676 Compared to controls (black datapoints), MG-Dep (orange datapoints) and –Repop (blue
677 datapoints) mice show a large increase in NREMS duration during the dark period both at
678 baseline and during recovery (n = 9 for control and MG-Depleted conditions and n = 6 for MG-
679 Repopulated condition, 2-way ANOVA, followed by Dunnett's test, *P < 0.05; **P < 0.01; ***P
680 < 0.001, orange and blue stars, significant differences between control and MG-Dep and MG-
681 Repop mice, respectively). Data points are shown in minutes per hour (min/h) and represent
682 the average of 2 h. (**F**) From left to right: Time in wakefulness (top) and NREMS (bottom)
683 during baseline light, dark and recovery light and dark periods (Mixed-effects analysis,
684 followed by Dunnett's test, *P < 0.05; **P < 0.01; ***P < 0.001). (**G**) Time-course of EEG delta
685 power (1–4 Hz) during the 3-day recording. EEG delta power is a proxy of sleep need. Both
686 MG-Dep and MG-Repop mice show deficiency in building up sleep need during the dark period
687 (2-way ANOVA, followed by Dunnett's test, *P < 0.05; **P < 0.01; ***P < 0.001, orange and
688 blue stars, significant differences between control and MG-Dep and MG-Repop mice,
689 respectively). (**H**) EEG power spectra of experimental mice in NREMS during baseline light
690 (left) and dark (right) periods. EEG power is expressed as % of baseline power of control
691 condition. Insets show amplification of specific EEG frequencies (2-way ANOVA, followed by
692 Dunnett's test, *P < 0.05; **P < 0.01; ***P < 0.001, orange and blue stars indicate significant
693 differences between control and MG-Depleted and MG-Repopulated mice, respectively). (**I**)
694 EEG power spectra of experimental mice in NREMS during recovery light (left) and dark (right)
695 periods. (**J**) Distribution of NREMS bout durations during baseline dark period across the
696 experimental mice. Sleep bout duration is represented on the x-axis (1-way ANOVA, followed
697 by Tukey test). (**K**) (Top) Representative time-frequency heatmap of spindles. (Bottom)
698 Representative EEG/EMG signals of a detected spindle. Dashed horizontal lines indicate
699 upper and lower thresholds used to detect spindles with wavelet energy within 9-16 Hz, and

700 dashed vertical lines indicate the start and end of the detected spindle. (**L**) Spindle rate during
701 NREMS episodes in different conditions. Spindle rate significantly decreased in MG-depleted
702 mice (mixed-effects analysis, followed by Dunnett's test, *P < 0.05; **P < 0.01; ***P < 0.001)).
703
704 **Figure 3. REMS regulation largely depends on the presence of the MG.** (**A**) Time-course
705 of REMS duration in control (black), MG-Dep (orange) and MG-Repop (blue) mouse groups.
706 MG-Dep mice exhibit a large increase in REMS time during the baseline dark period (n = 9 for
707 control and MG-Dep conditions and n = 6 for MG-Repop condition, 2-way ANOVA, followed
708 by Dunnett's test, *P < 0.05; **P < 0.01; ***P < 0.001, orange and blue stars represent
709 significant differences between control and MG-Dep and MG-Repop mice, respectively). Data
710 points are shown in minutes per hour (min/h) and represent the average of 2 h. (**B**) Time in
711 REMS during baseline dark period (mixed-effects analysis, followed by Dunnett's test, *P <
712 0.05; **P < 0.01; ***P < 0.001). (**C**) Distribution of REMs bout durations during baseline dark
713 period across 3 mouse groups. Sleep bout duration is presented as x-axis (1-way ANOVA,
714 followed by Tukey test). (**D**) EEG power spectra of all experimental mice in REMS during
715 baseline dark period. Insets show amplification for specific EEG frequencies (2-way ANOVA,
716 followed by Dunnett's test, *P < 0.05; **P < 0.01; ***P < 0.001, orange and blue stars are
717 significant differences between control mice and MG-Dep and MG-Repop mice respectively).
718 (**E**) Comodulogram graphs show the modulation index for a wide range of frequency pairs,
719 obtained from 12-h recordings of one animal in different conditions. (**F**) Normalized theta-
720 gamma coupling across 3 experimental conditions. Theta-gamma coupling is significantly
721 decreased in MG-depleted and -repopulated conditions (mixed-effects analysis, followed by
722 Dunnett's test, *P < 0.05; **P < 0.01; ***P < 0.001)).
723 .
724
725 **Figure 4. MG Repopulation fails to normalize the waking state deficits induced by MG**
726 **depletion.** (**A**) Time x frequency x power heatmap representations of the waking EEG of
727 control, MG-Dep and MG-Repop mice across the 3 recorded days (48 h baseline, 6 h sleep
728 deprivation and 18 h recovery) show large changes in higher frequency bands. (**B**) EEG power
729 spectra of experimental mice in wakefulness during baseline light and dark periods (2-way
730 ANOVA, followed by Dunnett's test, *P < 0.05; **P < 0.01; ***P < 0.001, orange star are
731 significant differences between control mice and MG-Dep mice). (**C**) Time-course of TDW
732 amounts indicates decreased TDW time during the dark period in MG-Dep and MG-Rep.
733 Datapoints are shown in min/h and represent the average of 2 h (baseline days 1 and 2 are
734 averaged), (2-way ANOVA followed by Dunnett's test, orange and blue stars are significant
735 differences between control and MG-Dep and MG-Repop mice, respectively). (**D**)
736 Quantification of time in TDW (min/h) during baseline light and dark period (mixed-effects

737 analysis, followed by Dunnett's test, *P < 0.05; **P < 0.01; ***P < 0.001). (**E**) Time in TDW
738 during SD. (**F**) Waking EEG slow-gamma (32-45 Hz) power dynamics during the 3-day
739 recording (baseline days 1 and 2 are averaged) (2-way ANOVA, followed by Dunnett's test).
740
741 **Figure 5. Large synaptic imbalance after MG depletion and repopulation.** (**A**) Schematic
742 illustration of the cell types for which the number of synapses was counted. NEUN (blue) and
743 PV (orange) positive neurons in the cortex and HCRT neurons in the hypothalamus. The
744 number of co-localized excitatory VGLUT1-HOMER1 synaptic proteins on NEUN, PV and
745 HCRT positive neurons were counted. Additionally, the number of co-localized inhibitory
746 SYT2-Gephyrin synaptic proteins on NEUN neurons were counted. (**B**) Representative image
747 depicting pre, postsynaptic proteins and their colocalization in a NEUN positive neuron.
748 Synapses (arrowheads) are marked with pink color using ImageJ macro (right). Scale bar:
749 10μm. (**C**) Number of VGLUT1-HOMER1 synapses/μm^2 of $NEUN^+$ soma. N=342 cells from
750 12 mice for control, 324 cells from 11 mice for MG-Dep, and 357 cells from 12 mice for MG-
751 Repop conditions. The data show a reduced number of these synapses in both MG-Dep and
752 MG-Repop conditions (**D**) Number of HOMER1 puncta/μm^2 of $NEUN^+$ soma. (**E**) Number of
753 VGLUT1 puncta/μm^2 of NEUN+ soma. (**F**) Number of SYT2-Gephyrin synapses/μm^2 of
754 $NEUN^+$ soma. N=299 cells from 12 mice for control, 270 cells from 11 mice for MG-Dep, and
755 306 cells from 12 mice for MG-Repop conditions. (**G**) Representative images depicting SYT2-
756 Gephyrin synapses in $NEUN^+$ cortical neuron. Large increase in these inhibitory synapses is
757 observed in the MG-Repop condition. Scale bar: 10 μm. (**H**) Distribution of PV^+ neurons (red)
758 in the cortex. Scale bar: 100 μm (left), 10 μm (right). (**I**) Number of vGLUT1-HOMER1
759 synapses/μm^2 of PV^+ soma. N=29 cells from 5 mice for control, 29 cells from 5 mice for MG-
760 Dep, and 23 cells from 4 mice for MG-Repop conditions. (**J**) Left, distribution of $HCRT^+$
761 neurons (red) in the lateral hypothalamus. Right, a $HCRT^+$ neuron stained with VGLUT1
762 (green) and HOMER1 (Cyan). Scale bar: 100 and 10 μm. (**K**) Number of VGLUT1-HOMER1
763 synapses/μm^2 of HCRT+ soma. N=70 cells from 3 mice for control, 73 cells from 3 mice for
764 MG-Dep, and 77 cells from 4 mice for MG-Repop conditions. (**L**) Gene expression of synaptic
765 proteins and neurotransmitter receptors at RNA level following MG depletion and repopulation.
766 N=3 for control and MG-Dep and n=4 for MG-Repop conditions. 1-way ANOVA, followed by
767 Tukey test, *P < 0.05; **P < 0.01; ***P < 0.001.
768
769 **Figure 6. MG repopulation largely restores the metabolite changes induced by**
770 **microglial depletion.** (**A**) PCA of targeted metabolites in cortex isolated from control (n=3),
771 MG depleted (n=3) and repopulated (n=4) mice. (**B**) LC-MS/MS assessment of the
772 neurotransmitter content in the brain of control, MG-Dep and MG-Repop mice. (**C**)

773 Downregulation of amino acids in the brain of experimental mice after MG depletion. 1-way
774 ANOVA, followed by Tukey test, *P < 0.05; **P < 0.01; ***P < 0.001.
775
776
777 **Figure S1: Transcriptional changes in microglial core genes following sleep**
778 **deprivation.** (**A**) Bar plots showing the expression of microglial core genes in the cortex and
779 hypothalamus under SD and NoSD (control) conditions. The color codes are provided. (**B**) Bar
780 plots showing the expression of the *Adrb2* gene. *P < 0.05; **P < 0.01; ***P < 0.001.

781 **Figure S2: Region and genotype specific transcriptional changes in microglial genes**
782 **following sleep deprivation.**

783 Heatmap showing differentially expressed genes in microglia of the cortex and hypothalamus
784 in WT and Ox-Ataxin mice under SD and control conditions. Each column represents microglia
785 data from one individual mouse, with 4-5 mice per group. The color code represents a linear
786 scale.

787

References

1. K. Ramar *et al.*, Sleep is essential to health: an American Academy of Sleep Medicine position statement. *J Clin Sleep Med* 10.5664/jcsm.9476 (2021).
2. A. A. Borbély, A two process model of sleep regulation. *Hum Neurobiol* **1**, 195-204 (1982).
3. G. F. Gilestro, G. Tononi, C. Cirelli, Widespread changes in synaptic markers as a function of sleep and wakefulness in Drosophila. *Science* **324**, 109-112 (2009).
4. S. Maret *et al.*, Homer1a is a core brain molecular correlate of sleep loss. *Proc Natl Acad Sci U S A* **104**, 20090-20095 (2007).
5. C. B. Saper, T. C. Chou, T. E. Scammell, The sleep switch: hypothalamic control of sleep and wakefulness. *Trends Neurosci* **24**, 726-731 (2001).
6. L. Amann, T. Masuda, M. Prinz, Mechanisms of myeloid cell entry to the healthy and diseased central nervous system. *Nat Immunol* **24**, 393-407 (2023).
7. K. Kierdorf, T. Masuda, M. J. C. Jordão, M. Prinz, Macrophages at CNS interfaces: ontogeny and function in health and disease. *Nat Rev Neurosci* **20**, 547-562 (2019).
8. M. Prinz, T. Masuda, M. A. Wheeler, F. J. Quintana, Microglia and Central Nervous System-Associated Macrophages-From Origin to Disease Modulation. *Annual review of immunology* **39**, 251-277 (2021).
9. M. Prinz, S. Jung, J. Priller, Microglia Biology: One Century of Evolving Concepts. *Cell* **179**, 292-311 (2019).
10. R. C. Paolicelli *et al.*, Synaptic pruning by microglia is necessary for normal brain development. *Science (New York, N.Y.)* **333**, 1456-1458 (2011).
11. K. Kierdorf *et al.*, Microglia emerge from erythromyeloid precursors via Pu.1- and Irf8-dependent pathways. *Nature neuroscience* **16**, 273-280 (2013).
12. C. Schulz *et al.*, A lineage of myeloid cells independent of Myb and hematopoietic stem cells. *Science (New York, N.Y.)* **336**, 86-90 (2012).
13. J. Bruttger *et al.*, Genetic Cell Ablation Reveals Clusters of Local Self-Renewing Microglia in the Mammalian Central Nervous System. *Immunity* **43**, 92-106 (2015).
14. T. L. Tay *et al.*, A new fate mapping system reveals context-dependent random or clonal expansion of microglia. *Nature neuroscience* **20**, 793-803 (2017).
15. Y. Huang *et al.*, Repopulated microglia are solely derived from the proliferation of residual microglia after acute depletion. *Nat Neurosci* **21**, 530-540 (2018).
16. M. J. Pinto *et al.*, Microglial TNFα orchestrates protein phosphorylation in the cortex during the sleep period and controls homeostatic sleep. *Embo j* **42**, e111485 (2023).
17. M. E. Choudhury *et al.*, Phagocytic elimination of synapses by microglia during sleep. *Glia* **68**, 44-59 (2020).
18. G. Corsi *et al.*, Microglia modulate hippocampal synaptic transmission and sleep duration along the light/dark cycle. *Glia* **70**, 89-105 (2022).
19. A. M. Ingiosi, M. R. Opp, J. M. Krueger, Sleep and immune function: glial contributions and consequences of aging. *Current opinion in neurobiology* **23**, 806-811 (2013).
20. L. H. Tuan, L. J. Lee, Microglia-mediated synaptic pruning is impaired in sleep-deprived adolescent mice. *Neurobiol Dis* **130**, 104517 (2019).
21. M. Bellesi *et al.*, Sleep Loss Promotes Astrocytic Phagocytosis and Microglial Activation in Mouse Cerebral Cortex. *J Neurosci* **37**, 5263-5273 (2017).
22. A. Drieu *et al.*, Parenchymal border macrophages regulate the flow dynamics of the cerebrospinal fluid. *Nature* **611**, 585-593 (2022).
23. Y. W. Zhang, R. Thompson, H. Zhang, H. Xu, APP processing in Alzheimer's disease. *Mol Brain* **4**, 3 (2011).
24. J. Hara *et al.*, Genetic ablation of orexin neurons in mice results in narcolepsy, hypophagia, and obesity. *Neuron* **30**, 345-354 (2001).
25. A. Vassalli, P. Franken, Hypocretin (orexin) is critical in sustaining theta/gamma-rich waking behaviors that drive sleep need. *Proc Natl Acad Sci U S A* **114**, E5464-e5473 (2017).

26. N. N. Dagher *et al.*, Colony-stimulating factor 1 receptor inhibition prevents microglial plaque association and improves cognition in 3xTg-AD mice. *J Neuroinflammation* **12**, 139 (2015).
27. H. Van Hove *et al.*, A single-cell atlas of mouse brain macrophages reveals unique transcriptional identities shaped by ontogeny and tissue environment. *Nat Neurosci* **22**, 1021-1035 (2019).
28. A. Seifinejad, S. Li, M. L. Possovre, A. Vassalli, M. Tafti, Hypocretinergic interactions with the serotonergic system regulate REM sleep and cataplexy. *Nat Commun* **11**, 6034 (2020).
29. M. Bandarabadi *et al.*, A role for spindles in the onset of rapid eye movement sleep. *Nat Commun* **11**, 5247 (2020).
30. M. Bandarabadi *et al.*, Dynamic modulation of theta-gamma coupling during rapid eye movement sleep. *Sleep* **42**, 1-11 (2019).
31. T. Endo *et al.*, Selective REM sleep deprivation in humans: effects on sleep and sleep EEG. *Am J Physiol* **274**, R1186-1194 (1998).
32. G. Tononi, C. Cirelli, Sleep and synaptic homeostasis: a hypothesis. *Brain Res Bull* **62**, 143-150 (2003).
33. I. Hristovska *et al.*, Sleep decreases neuronal activity control of microglial dynamics in mice. *Nat Commun* **13**, 6273 (2022).
34. K. Kon *et al.*, Cortical parvalbumin neurons are responsible for homeostatic sleep rebound through CaMKII activation. *bioRxiv* 10.1101/2023.04.29.537929, 2023.2004.2029.537929 (2023).
35. B. Bouhours, E. Gjoni, O. Kochubey, R. Schneggenburger, Synaptotagmin2 (Syt2) Drives Fast Release Redundantly with Syt1 at the Output Synapses of Parvalbumin-Expressing Inhibitory Neurons. *J Neurosci* **37**, 4604-4617 (2017).
36. M. Bellesi *et al.*, Effects of sleep and wake on oligodendrocytes and their precursors. *The Journal of neuroscience : the official journal of the Society for Neuroscience* **33**, 14288-14300 (2013).
37. M. Bellesi, L. de Vivo, G. Tononi, C. Cirelli, Effects of sleep and wake on astrocytes: clues from molecular and ultrastructural studies. *BMC biology* **13**, 66 (2015).
38. S. Dujardin *et al.*, Tau molecular diversity contributes to clinical heterogeneity in Alzheimer's disease. *Nat Med* **26**, 1256-1263 (2020).
39. N. Naidoo, Cellular stress/the unfolded protein response: relevance to sleep and sleep disorders. *Sleep Med Rev* **13**, 195-204 (2009).
40. L. Rajendran, R. C. Paolicelli, Microglia-Mediated Synapse Loss in Alzheimer's Disease. *J Neurosci* **38**, 2911-2919 (2018).
41. J. H. Roh *et al.*, Potential role of orexin and sleep modulation in the pathogenesis of Alzheimer's disease. *The Journal of experimental medicine* **211**, 2487-2496 (2014).
42. A. Gabelle *et al.*, Reduced brain amyloid burden in elderly patients with narcolepsy type 1. *Ann Neurol* **85**, 74-83 (2019).
43. Y. L. Tan, Y. Yuan, L. Tian, Microglial regional heterogeneity and its role in the brain. *Mol Psychiatry* **25**, 351-367 (2020).
44. P. Ayata *et al.*, Epigenetic regulation of brain region-specific microglia clearance activity. *Nat Neurosci* **21**, 1049-1060 (2018).
45. S. R. Morairty *et al.*, A role for cortical nNOS/NK1 neurons in coupling homeostatic sleep drive to EEG slow wave activity. *Proc Natl Acad Sci U S A* **110**, 20272-20277 (2013).
46. C. Cirelli, R. Huber, A. Gopalakrishnan, T. L. Southard, G. Tononi, Locus ceruleus control of slow-wave homeostasis. *J Neurosci* **25**, 4503-4511 (2005).
47. E. F. Willis *et al.*, Repopulating Microglia Promote Brain Repair in an IL-6-Dependent Manner. *Cell* **180**, 833-846.e816 (2020).
48. Y. Zhang *et al.*, Repopulating retinal microglia restore endogenous organization and function under CX3CL1-CX3CR1 regulation. *Sci Adv* **4**, eaap8492 (2018).

890 49. E. Favuzzi *et al.*, GABA-receptive microglia selectively sculpt developing inhibitory circuits.
891 *Cell* **184**, 4048-4063.e4032 (2021).
892 50. D. K. Wilton, L. Dissing-Olesen, B. Stevens, Neuron-Glia Signaling in Synapse Elimination.
893 *Annu Rev Neurosci* **42**, 107-127 (2019).
894 51. A. Badimon *et al.*, Negative feedback control of neuronal activity by microglia. *Nature* **586**,
895 417-423 (2020).
896 52. M. C. C. Guillaumin *et al.*, Deficient synaptic neurotransmission results in a persistent sleep-
897 like cortical activity across vigilance states in mice. *bioRxiv* 10.1101/2023.05.11.540034,
898 2023.2005.2011.540034 (2023).
899 53. A. Seifinejad, A. Vassalli, M. Tafti, Neurobiology of cataplexy. *Sleep Med Rev* **60**, 101546
900 (2021).
901 54. A. Osorio-Forero *et al.*, Noradrenergic circuit control of non-REM sleep substates. *Current*
902 *biology : CB* **31**, 5009-5023.e5007 (2021).
903 55. C. Ma *et al.*, Microglia Regulate Sleep via Calcium-Dependent Modulation of Norepinephrine
904 Transmission. *bioRxiv* 10.1101/2023.07.24.550176, 2023.2007.2024.550176 (2023).
905 56. C. Ma *et al.*, Microglia regulate sleep through calcium-dependent modulation of
906 norepinephrine transmission. *Nat Neurosci* **27**, 249-258 (2024).
907 57. R. D. Stowell *et al.*, Noradrenergic signaling in the wakeful state inhibits microglial
908 surveillance and synaptic plasticity in the mouse visual cortex. *Nat Neurosci* **22**, 1782-1792
909 (2019).
910 58. Y. U. Liu *et al.*, Neuronal network activity controls microglial process surveillance in awake
911 mice via norepinephrine signaling. *Nat Neurosci* **22**, 1771-1781 (2019).
912 59. M. Maugard, P. A. Vigneron, J. P. Bolanos, G. Bonvento, l-Serine links metabolism with
913 neurotransmission. *Prog Neurobiol* **197**, 101896 (2021).
914 60. K. Vávrová, A. Hrabálek, P. Dolezal, T. Holas, J. Zbytovská, L-Serine and glycine based
915 ceramide analogues as transdermal permeation enhancers: polar head size and hydrogen
916 bonding. *Bioorg Med Chem Lett* **13**, 2351-2353 (2003).
917 61. H. Liu *et al.*, Microglia modulate stable wakefulness via the thalamic reticular nucleus in
918 mice. *Nat Commun* **12**, 4646 (2021).
919 62. T. Masuda *et al.*, Novel Hexb-based tools for studying microglia in the CNS. *Nat Immunol* **21**,
920 802-815 (2020).
921 63. T. Masuda *et al.*, Specification of CNS macrophage subsets occurs postnatally in defined
922 niches. *Nature* **604**, 740-748 (2022).
923 64. F. Lei *et al.*, CSF1R inhibition by a small-molecule inhibitor is not microglia specific; affecting
924 hematopoiesis and the function of macrophages. *Proc Natl Acad Sci U S A* **117**, 23336-23338
925 (2020).
926 65. C. Mezö *et al.*, Different effects of constitutive and induced microbiota modulation on
927 microglia in a mouse model of Alzheimer's disease. *Acta neuropathologica communications*
928 **8**, 119 (2020).
929 66. O. Mossad *et al.*, Gut microbiota drives age-related oxidative stress and mitochondrial
930 damage in microglia via the metabolite N(6)-carboxymethyllysine. *Nature neuroscience* **25**,
931 295-305 (2022).
932 67. A. Dobin *et al.*, STAR: ultrafast universal RNA-seq aligner. *Bioinformatics* **29**, 15-21 (2013).
933 68. J. Harrow *et al.*, GENCODE: the reference human genome annotation for The ENCODE
934 Project. *Genome Res* **22**, 1760-1774 (2012).
935 69. M. E. Ritchie *et al.*, limma powers differential expression analyses for RNA-sequencing and
936 microarray studies. *Nucleic Acids Res* **43**, e47 (2015).
937 70. S. X. Ge, D. Jung, R. Yao, ShinyGO: a graphical gene-set enrichment tool for animals and
938 plants. *Bioinformatics* **36**, 2628-2629 (2020).
939 71. E. Favuzzi *et al.*, GABA-receptive microglia selectively sculpt developing inhibitory circuits.
940 *Cell* **184**, 5686 (2021).

941 72. S. Behringer *et al.*, Targeted Metabolic Profiling of Methionine Cycle Metabolites and Redox
942 Thiol Pools in Mammalian Plasma, Cells and Urine. *Metabolites* **9** (2019).
943 73. A. C. Bravo *et al.*, Analysis of S-Adenosylmethionine and S-Adenosylhomocysteine: Method
944 Optimisation and Profiling in Healthy Adults upon Short-Term Dietary Intervention.
945 *Metabolites* **12**, 373 (2022).
946 74. L. Hannibal *et al.*, Metabolic Profiling in Human Fibroblasts Enables Subtype Clustering in
947 Glycogen Storage Disease. *Front Endocrinol (Lausanne)* **11**, 579981 (2020).
948 75. J. P. Maier *et al.*, Inhibition of metabotropic glutamate receptor III facilitates sensitization to
949 alkylating chemotherapeutics in glioblastoma. *Cell Death Dis* **12**, 723 (2021).
950 76. L. Moritz, K. Klotz, S. C. Grunert, L. Hannibal, U. Spiekerkoetter, Metabolic phenotyping in
951 phenylketonuria reveals disease clustering independently of metabolic control. *Mol Genet*
952 *Metab* **138**, 107509 (2023).
953 77. P. Franken, A. Malafosse, M. Tafti, Genetic variation in EEG activity during sleep in inbred
954 mice. *Am J Physiol* **275**, R1127-1137 (1998).
955 78. S. Li, P. Franken, A. Vassalli, Bidirectional and context-dependent changes in theta and
956 gamma oscillatory brain activity in noradrenergic cell-specific Hypocretin/Orexin receptor 1-
957 KO mice. *Sci Rep* **8**, 15474 (2018).
958 79. A. B. Tort *et al.*, Dynamic cross-frequency couplings of local field potential oscillations in rat
959 striatum and hippocampus during performance of a T-maze task. *Proc Natl Acad Sci U S A*
960 **105**, 20517-20522 (2008).

961

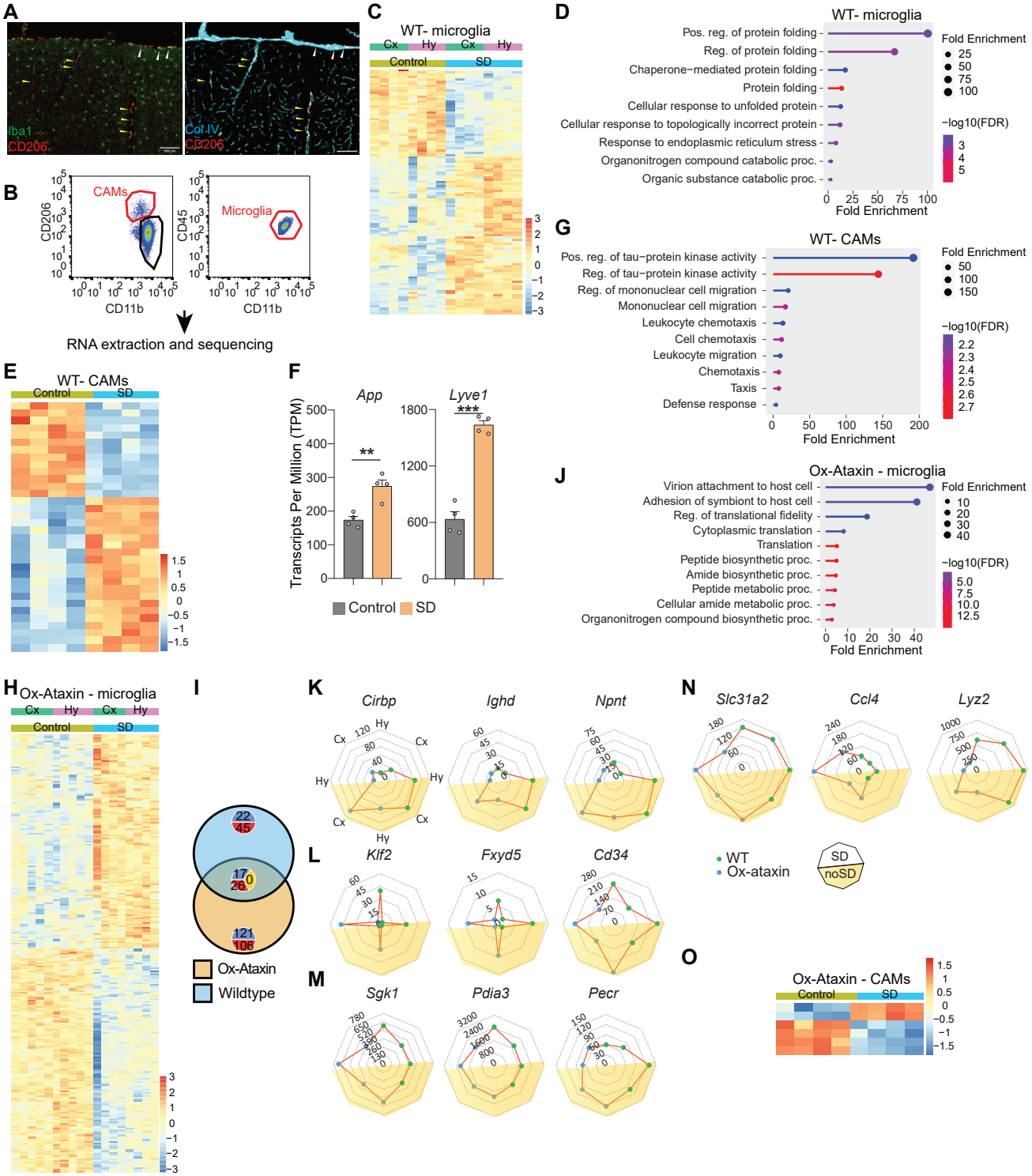
A
Iba1
CD206
Col IV
CD206
B
CAMs
Microglia
CD206
CD45
CD11b
CD11b
RNA extraction and sequencing
C
WT- microglia
Cx
Hy
Cx
Hy
Control
SD
D
WT- microglia
Pos. reg. of protein folding
Reg. of protein folding
Chaperone−mediated protein folding
Protein folding
Cellular response to unfolded protein
Cellular response to topologically incorrect protein
Response to endoplasmic reticulum stress
Organonitrogen compound catabolic proc.
Organic substance catabolic proc.
Fold Enrichment
−log10(FDR)
Fold Enrichment
E
WT- CAMs
Control
SD
F
App
Lyve1
Transcripts Per Million (TPM)
Control
SD
G
WT- CAMs
Pos. reg. of tau−protein kinase activity
Reg. of tau−protein kinase activity
Reg. of mononuclear cell migration
Mononuclear cell migration
Leukocyte chemotaxis
Cell chemotaxis
Leukocyte migration
Chemotaxis
Taxis
Defense response
Fold Enrichment
−log10(FDR)
Fold Enrichment
J
Ox-Ataxin - microglia
Virion attachment to host cell
Adhesion of symbiont to host cell
Reg. of translational fidelity
Cytoplasmic translation
Translation
Peptide biosynthetic proc.
Amide biosynthetic proc.
Peptide metabolic proc.
Cellular amide metabolic proc.
Organonitrogen compound biosynthetic proc.
Fold Enrichment
−log10(FDR)
Fold Enrichment
H
Ox-Ataxin - microglia
Cx
Hy
Cx
Hy
Control
SD
I
Ox-Ataxin
Wildtype
K
Cirbp
Ighd
Npnt
L
Klf2
Fxyd5
Cd34
M
Sgk1
Pdia3
Pecr
N
Slc31a2
Ccl4
Lyz2
WT
Ox-ataxin
SD
noSD
O
Ox-Ataxin - CAMs
Control
SD

Figure 1

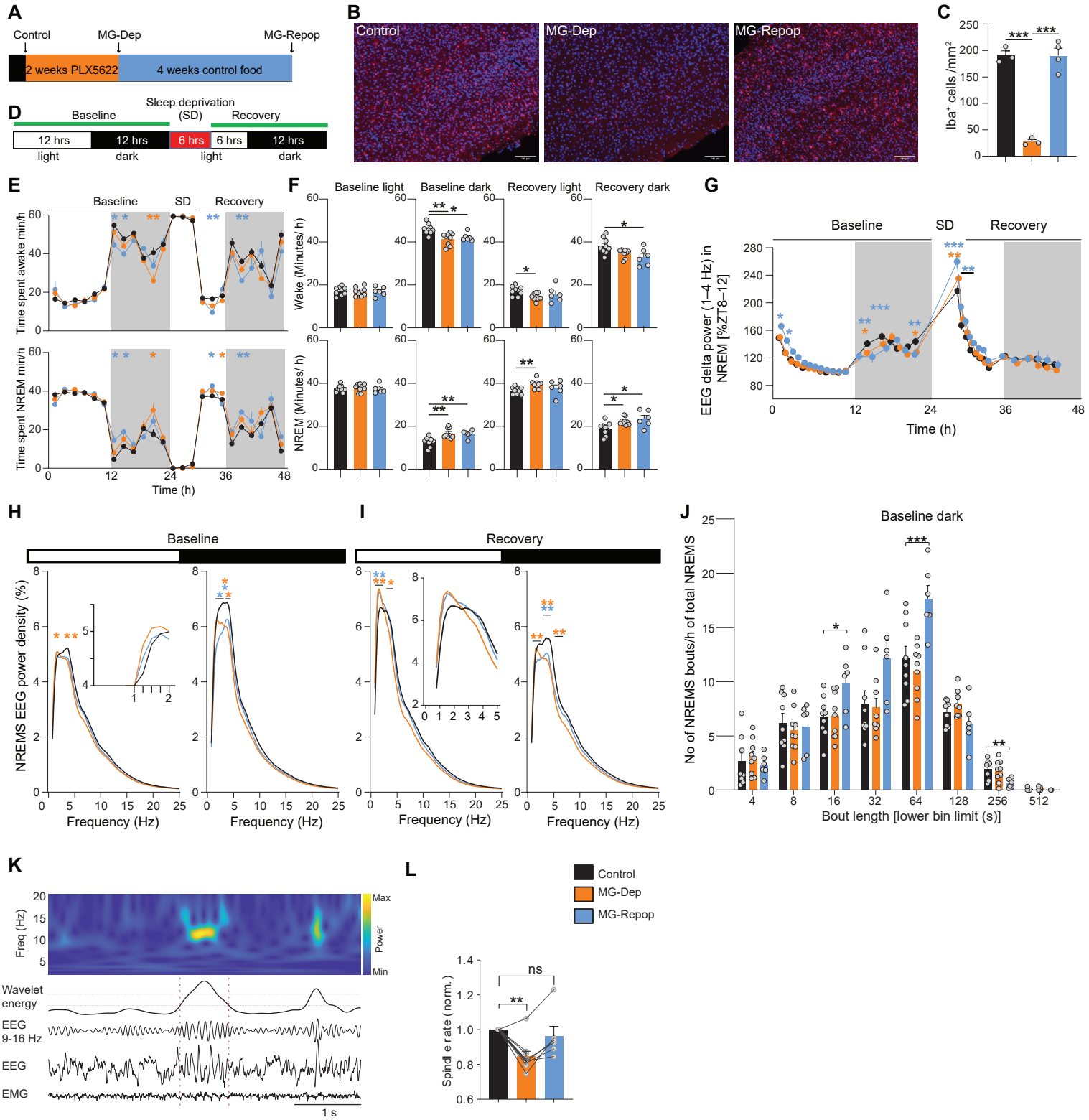
A
Control
MG-Dep
MG-Repop
2 weeks PLX5622
4 weeks control food
D
Baseline
Sleep deprivation (SD)
Recovery
12 hrs light
12 hrs dark
6 hrs light
6 hrs
12 hrs dark
B
Control
MG-Dep
MG-Repop
C
Iba+ cells /mm2
E
Baseline
SD
Recovery
Time spent awake min/h
Time spent NREM min/h
Time (h)
F
Baseline light
Baseline dark
Recovery light
Recovery dark
Wake (Minutes/ h)
NREM (Minutes/ h)
G
EEG delta power (1–4 Hz) in NREM [%ZT8–12]
Time (h)
H
Baseline
NREMS EEG power density (%)
Frequency (Hz)
I
Recovery
Frequency (Hz)
J
Baseline dark
No of NREMS bouts/h of total NREMS
Bout length [lower bin limit (s)]
K
Freq (Hz)
Max
Power
Min
Wavelet energy
EEG 9-16 Hz
EEG
EMG
1 s
L
Control
MG-Dep
MG-Repop
ns
Spindle rate (norm.)

Figure 2

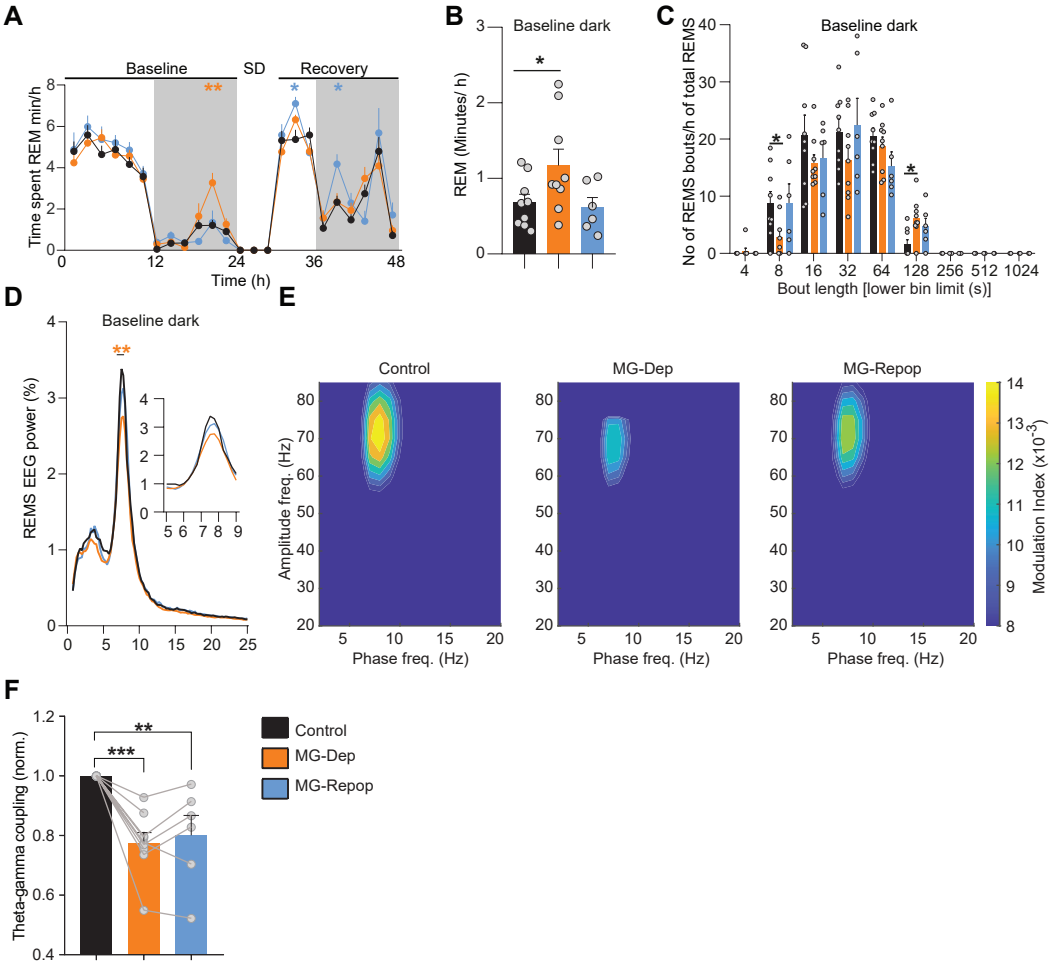
A
Baseline
SD
Recovery
Time spent REM min/h
Time (h)
B
Baseline dark
REM (Minutes/ h)
C
Baseline dark
No of REMS bouts/h of total REMS
Bout length [lower bin limit (s)]
D
Baseline dark
REMS EEG power (%)
E
Control
MG-Dep
MG-Repop
Amplitude freq. (Hz)
Phase freq. (Hz)
Modulation Index (x10-3)
F
Theta-gamma coupling (norm.)
Control
MG-Dep
MG-Repop

Figure 3

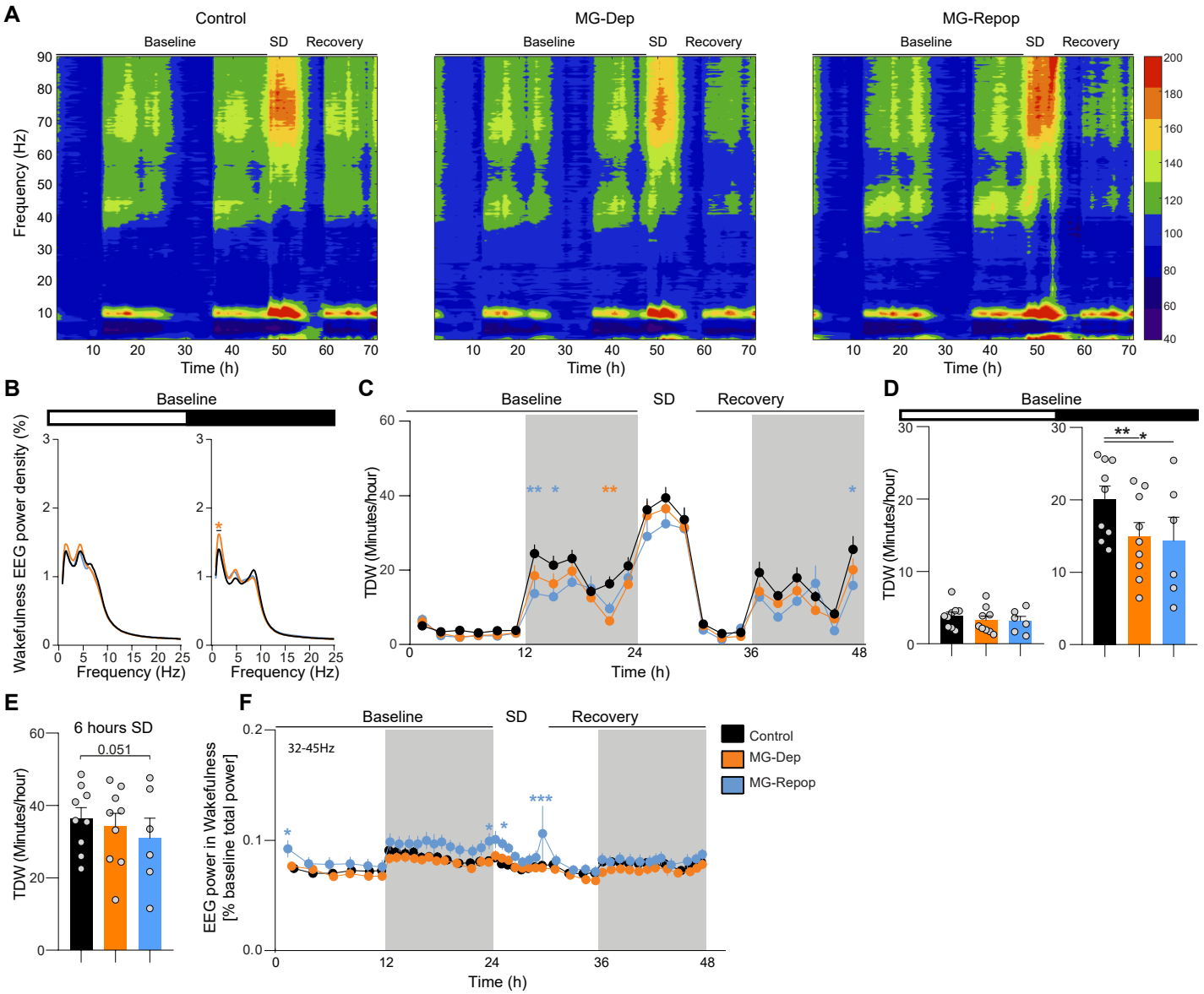
A
Control
MG-Dep
MG-Repop
Baseline
SD
Recovery
Frequency (Hz)
Time (h)
B
Wakefulness EEG power density (%)
Frequency (Hz)
C
TDW (Minutes/hour)
D
E
6 hours SD
0.051
F
32-45Hz
EEG power in Wakefulness [% baseline total power]
Control
MG-Dep
MG-Repop

Figure 4

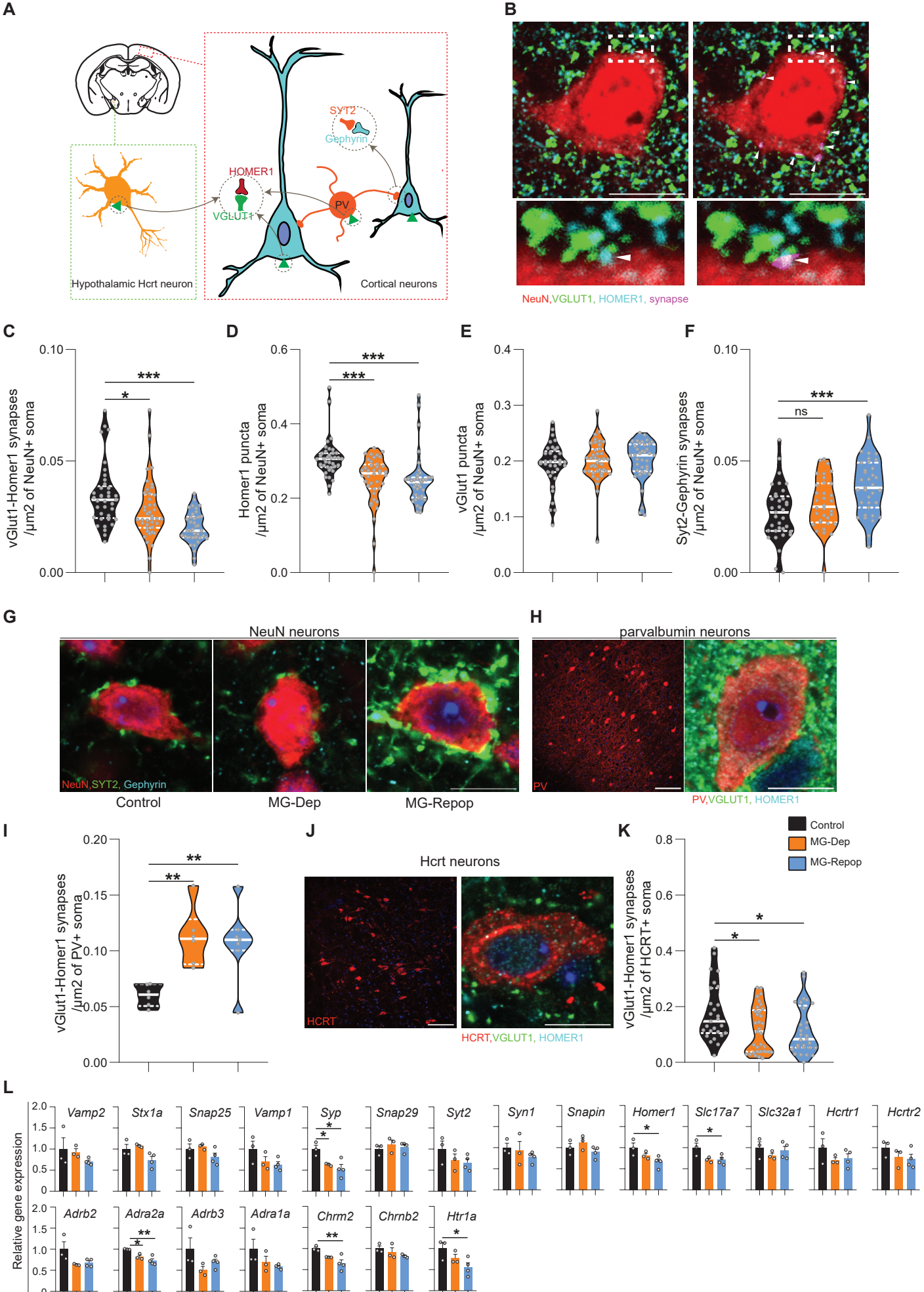
A
SYT2
Gephyrin
HOMER1
VGLUT1
PV
Hypothalamic Hcrt neuron
Cortical neurons
B
NeuN,VGLUT1, HOMER1, synapse
C
vGlut1-Homer1 synapses /µm2 of NeuN+ soma
D
Homer1 puncta /µm2 of NeuN+ soma
E
vGlut1 puncta /µm2 of NeuN+ soma
F
Syt2-Gephyrin synapses /µm2 of NeuN+ soma
ns
G
NeuN neurons
NeuN,SYT2, Gephyrin
Control
MG-Dep
MG-Repop
H
parvalbumin neurons
PV
PV,VGLUT1, HOMER1
I
vGlut1-Homer1 synapses /µm2 of PV+ soma
J
Hcrt neurons
HCRT
HCRT,VGLUT1, HOMER1
K
Control
MG-Dep
MG-Repop
vGlut1-Homer1 synapses /µm2 of HCRT+ soma
L
Relative gene expression
Vamp2
Stx1a
Snap25
Vamp1
Syp
Snap29
Syt2
Syn1
Snapin
Homer1
Slc17a7
Slc32a1
Hcrtr1
Hcrtr2
Adrb2
Adra2a
Adrb3
Adra1a
Chrm2
Chrnb2
Htr1a

Figure 5

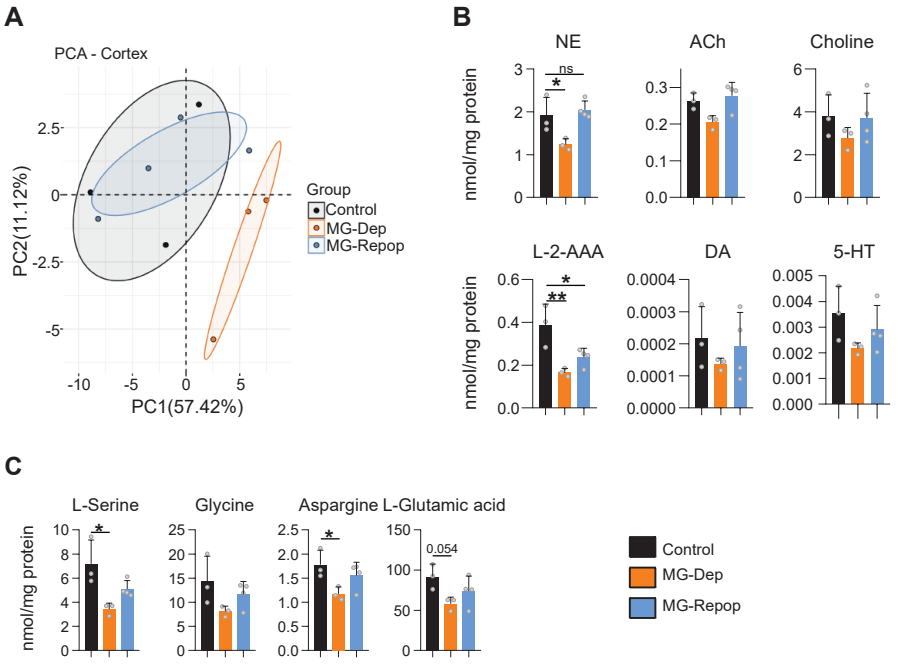
A
PCA - Cortex
PC2(11.12%)
PC1(57.42%)
Group
Control
MG-Dep
MG-Repop
B
NE
ACh
Choline
L-2-AAA
DA
5-HT
nmol/mg protein
ns
*
**
C
L-Serine
Glycine
Aspargine
L-Glutamic acid
0.054
Control
MG-Dep
MG-Repop

Figure 6

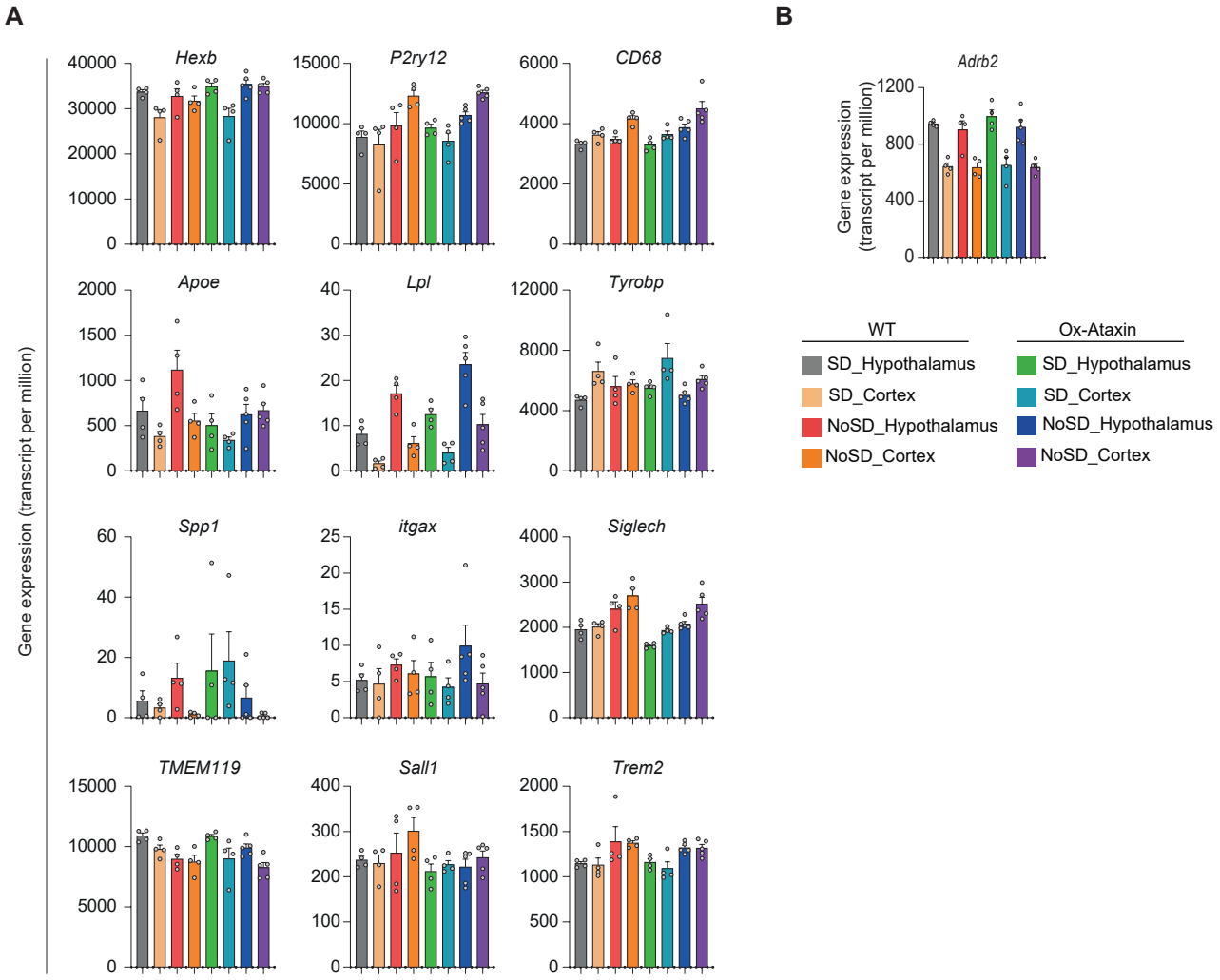
A
B
Gene expression (transcript per million)
Hexb
P2ry12
CD68
Apoe
Lpl
Tyrobp
Spp1
itgax
Siglech
TMEM119
Sall1
Trem2
Adrb2
WT
Ox-Ataxin
SD_Hypothalamus
SD_Cortex
NoSD_Hypothalamus
NoSD_Cortex

Figure S1

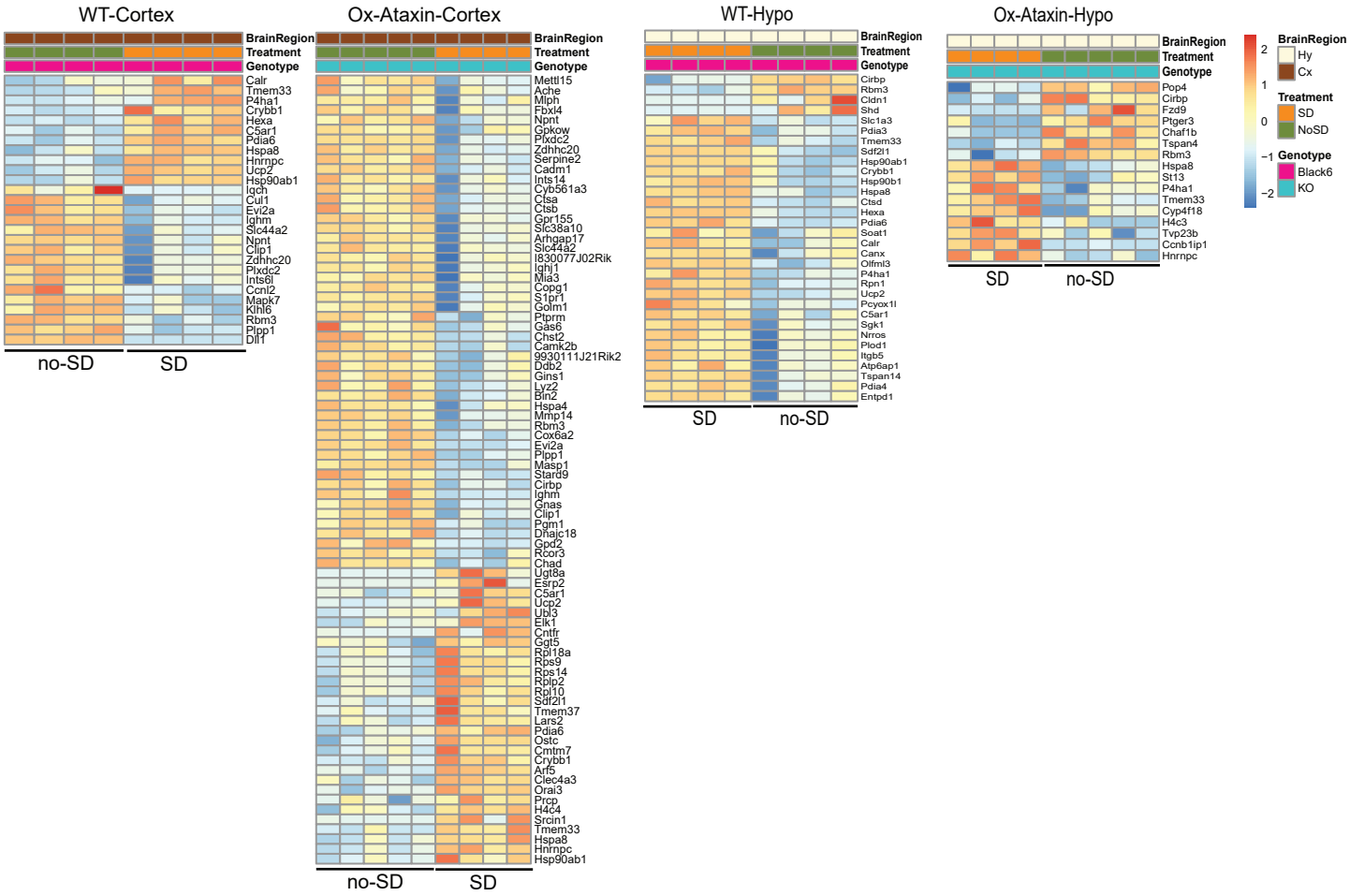
WT-Cortex
Ox-Ataxin-Cortex
WT-Hypo
Ox-Ataxin-Hypo
BrainRegion
Treatment
Genotype
no-SD
SD
Hy
Cx
NoSD
Black6
KO

Figure S2